METALLIC SCATTERING LIFETIME MEASUREMENTS WITH TERAHERTZ TIME-DOMAIN SPECTROSCOPY

by

Graham Bryce Lea

B.Sc. (Hons.), McGill University, 2006

a Thesis submitted in partial fulfillment
of the requirements for the degree of
Master of Science
in the Department
of
Physics

SIMON FRASER UNIVERSITY
Spring 2010

APPROVAL

Name: Graham Bryce Lea

Degree: Master of Science

Title of Thesis: Metallic scattering lifetime measurements with terahertz time-domain spectroscopy

Examining Committee: Dr. David Broun, Associate Professor, Physics,
Simon Fraser University
Chair

Dr. J. Steven Dodge, Associate Professor, Physics,
Simon Fraser University: Senior Supervisor

Dr. Igor Herbut, Professor, Physics,
Simon Fraser University: Supervisor

Dr. Jeff Sonier, Professor, Physics,
Simon Fraser University: Supervisor

Dr. Erol Girt, Associate Professor, Physics,
Simon Fraser University: Internal Examiner

Date Approved: January 25, 2010

Declaration of
Partial Copyright Licence

Abstract

The momentum scattering lifetime is a fundamental parameter of metallic conduction that can be measured with terahertz time-domain spectroscopy. This technique has an important strength over optical reflectance spectroscopy: it is capable of measuring both the phase and the amplitude of the probing radiation. This allows simultaneous, independent measurements of the scattering lifetime and resistivity. Broadly, it is the precision of the phase measurement that determines the precision of scattering lifetime measurements. This thesis describes milliradian-level phase measurement refinements in the experimental technique and measures the conductivity anisotropy in the correlated electron system $CaRuO_3$. These phase measurement refinements translate to femtosecond-level refinements in scattering lifetime measurements of thin metallic films.

Keywords: terahertz time-domain spectroscopy, calcium ruthenate, ruthenium oxides, correlated electrons, experimental technique.

For Dad, Mom, Ellen, and Alexander.
I'm proud to have you guys as family.

"Some people may sit back and say, 'I want to solve this problem' and they sit down and say, 'How do I solve this problem?' I don't. I just move around in the mathematical waters, thinking about things, being curious, interested, talking to people, stirring up ideas; things emerge and I follow them up. Or I see something which connects up with something else I know about, and I try to put them together and things develop. I have practically never started out with any idea of what I'm going to be doing or where it's going to go."

— *Michael F. Atiyah*

Acknowledgments

There are many people without whom this thesis would not have been possible.

My family has been wonderful during the course of this work, as they have always been. They continually provided the encouragement to persevere when times were tough, the lessons on self-motivation that every grad student needs, and the repeated advice "not to beat myself up" over the problems that often weren't even under my control.

I'd like to thank my senior supervisor, Steve Dodge, with whom it was easy to talk about anything of interest. This was complemented by his high expectations of me to take charge of my own research, which might have been the most important lesson that I will take away from this degree.

Chang-Beom Eom and the Oxide Laboratory and the University of Wisconsin-Madison provided the $CaRuO_3$ samples and helped with many crystallography questions.

My colleagues in the Dodge lab were always a lot of fun to work with. I'd like to thank Amir Farahani for answering my myriad of questions about terahertz time-domain spectroscopy and to him, Payam Mousavi, Jesse Petersen, and Stéphane Savard for good companionship in the lab and out of it. Learning bits of Persian culture on a weekly basis was great too.

Bryan Gormann, Ken Myrtle, and Vic Allen were very helpful with the technical side of working in physics, always gracefully putting their own work on hold to help me with whatever problem I had in the lab.

Kerry O'Donoghue cheerfully volunteered to proofread this work, wielding her knowledge of "real" English grammar to make the writing more porfessional... err... "professional".

Finally, I'd like to thank all of my friends for the jovial relief they always provided. In particular, in the final months of this degree, it has been wonderful to get closer to Fumie Odette, whose love, warmth, and support has been so uplifting.

Contents

List of Figures

Chapter 1

Terahertz time-domain spectroscopy

Many of the recent developments in condensed matter physics have been extracted from the study of quasiparticle excitations. Exciting a system out of its ground state by optical, thermal, and other means opens a window into its fundamental interactions, giving physicists the opportunity to test the limits of their most important theories.

These excitations span a wide energy range — much wider than any one experimental technique can probe. Spectroscopic techniques at microwave and optical frequencies have been employed for many decades, but extending their spectral ranges to the "terahertz gap" in between proved difficult for a long time [13]. Lattice vibrations, excitons, and quasiparticle scattering rates are examples of the many important excitations in correlated electron systems that lie in this terahertz (THz) regime. Therefore, bridging this gap was an important challenge for experimental physicists. The advent of photoconducting, silicon on sapphire dipole antennas [2, 22, 51, 23, 29] was a seed for new experimental techniques that could indeed probe the terahertz spectrum. Now a host of other coherent terahertz radiation sources exist, such as gallium arsenide antennas and optical rectification.

One such experimental technique is terahertz time-domain spectroscopy (THz-TDS), which measures the probing terahertz pulses in a manner that is sensitive to their phase. Typically, the terahertz pulses are transmitted through a dielectric, metal, or superconducting film, which leads to the simultaneous measurement of both the real and imaginary parts of a sample's optical conductivity $\tilde{\sigma}(\omega) = \sigma_1(\omega) + i\sigma_2(\omega)$, without the use of Kramers-Kronig

relations. This phase-sensitivity allows researchers to measure pairs of transport properties at once, such as the resistivity ρ and scattering lifetime τ in metals, or the quasiparticle and condensate fractions in superconductors.

1.1 Principles of terahertz generation

Our terahertz pulses are generated by near-infrared (NIR), femtosecond laser pulses incident on a photoconducting dipole antenna. Here I outline the details of femtosecond pulse generation and how the pulses induce the antenna to emit terahertz radiation.

1.1.1 Mode-locked lasers

Our terahertz pulses are generated by the picosecond dynamics of the antennas. Consequently, we require that the antennas be stimulated into this emissive state on an even shorter timescale; we use mode-locked femtosecond laser pulses to do this.

Mode-locking is the process of fixing the phase of each mode in a laser cavity in relation to its neighbouring modes so that ultrashort pulses are generated. Theoretically, a laser cavity of length $2L$ supports an infinite number of modes that are equally spaced in frequency by $\Delta\nu = c/2L$. When these modes are also equally spaced in phase, they constructively interfere to form short, intense bursts at a repetition rate equal to the fundamental frequency of the cavity $c/2L$, as in Figure 1.1. Mathematically, these short pulses are related to the Dirichlet kernel,

$$D_N(x) = \sum_{n=-N}^{N} e^{inx} = 1 + 2\sum_{n=1}^{N} \cos(nx) = \frac{\sin\left[(N+\frac{1}{2})x\right]}{\sin(x/2)}, \tag{1.1}$$

which is small where x is not a multiple of 2π and large where it is. The number of modes that actually lase is limited by the laser's gain bandwidth. Constructing a $T_{\text{pulse}} = 100$ fs pulse from a cavity with a round-trip time of $T_{\text{cavity}} = 2L/c \simeq 10$ ns requires $N = T_{\text{cavity}}/T_{\text{pulse}} \simeq 100,000$ modes. Choosing a gain medium with a broad absorption band like titanium-sapphire (Ti:Sapph) thus becomes essential.

In our system, the mode-locked state is induced via Kerr self-focusing. The Kerr effect results in a Ti:Sapph crystal index of refraction that depends on the cavity beam's intensity profile $I(x)$: $n(x) = n_0 + n_2 I(x)$. This focuses the beam by increasing the path length of its central ray, just as the path length of a central ray is increased through a convex

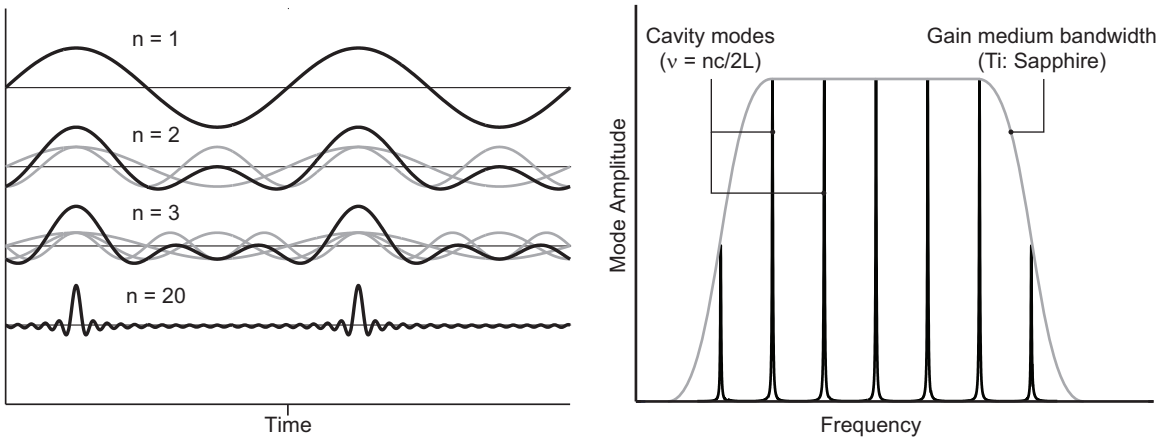

Figure 1.1: Principles of mode-locking. Left: mode-locking occurs when superimposed modes are equally spaced in both frequency and phase. The top waveform is the laser cavity's fundamental frequency $\nu = c/2L$. In the second and third waveforms from the top, two and three grey modes of frequency ν and 2ν (and 3ν) are separated by a phase of $\pi/2$ and superimposed. At the bottom, twenty modes are superimposed to form a short-duration pulse (constituent modes not shown). Right: the infinite number of modes at frequencies $nc/2L$ are enveloped by the laser's gain bandwidth (mode frequency spacing greatly exaggerated).

lens. This comparison is best seen using Fermat's principle for the convex lens, rather than Snell's law — see Figure 1.2. The Kerr self-focusing results in mode-locking by amplifying short, high-intensity pulses at the expense of longer pulses. The laser cavity is bistable in continuous-wave (unpulsed) and pulsed modes, so snapping a prism in the cavity pushes it into the pulsed mode.

1.1.2 Dipole antennas

Both our terahertz source and detector are Auston switch dipole antennas etched onto silicon-on-sapphire wafers (Figure 1.3) [2, 23, 51]. Femtosecond laser pulses are focused

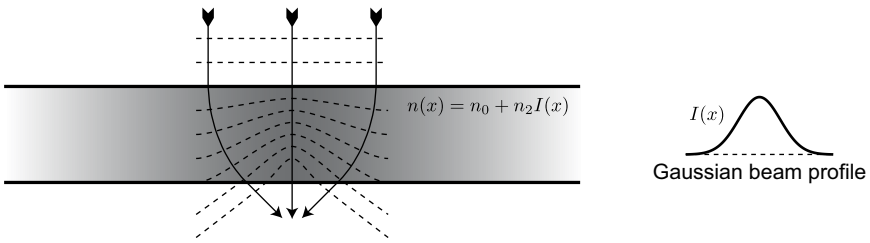

Figure 1.2: Kerr self-focusing. For high-intensity light, the Kerr effect induces an intensity-dependent index of refraction $n(x) = n_0 + n_2 I(x)$. If, for example, a Gaussian beam with intensity $I(x)$ is incident on the medium, then its central rays will experience a greater path length than its outer rays and the beam will be focused.

onto a micron-sized pad of photoconducting silicon that bridges two metal strips. These pulses create photocarriers in the silicon and a bias applied across the antenna results in a current pulse j whose duration is limited by the photocarrier lifetime. This transient current radiates into free space with a time-domain amplitude $E(t) \propto \frac{\partial j}{\partial t}$ [2].

A remarkable symmetry in THz-TDS is that the same dipole antennas that generate the terahertz pulses can be used to detect them. In this case, the femtosecond laser pulses serve to take time-domain "snapshots" of a photocurrent that gets driven by the incident terahertz pulses. I elaborate on our detection scheme in Section 1.2.8.

1.2 Apparatus

A mode-locked Ti:Sapph laser drives our THz-TDS setup, illustrated in Figure 1.4. The laser is split into two beam arms—one for the THz emitter and one for the detector. After the THz radiation is emitted, it is collimated and focused by off-axis paraboloid mirrors through a sample held within a cryostat. Two more off-axis parabolic mirrors collimate and focus the transmitted radiation onto the detector antenna. The emitter arm of the laser beam has a delay stage that can vary the length of the arm by ~ 20 mm (~ 67 ps), which is more than adequate for finding and sampling the entire length of the transmitted terahertz pulse. Here I outline the details of these different elements.

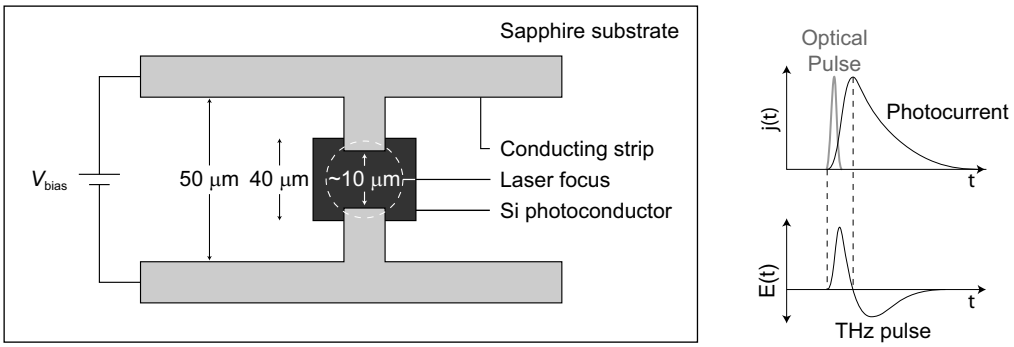

Figure 1.3: Schematic of our photoconducting silicon-on-sapphire antennas. Femtosecond laser pulses are focused to an area of photoconducting silicon that bridges two metal contacts, across which a bias is applied. Together, the intermittent laser pulses and bias generate transient photocurrents that produce single-cycle terahertz pulses according to $E(t) \propto dj/dt$ (shown on right).

1.2.1 Laser

We use a Kapteyn-Murnane Labs Ti:Sapph laser to stimulate our antennas. The laser pulses are approximately 80 fs in duration, have a center wavelength of 800 nm and a spectral width of $\sim$ 30 nm. Of the 500 mW of total power emitted by this laser, 250 mW is used for the THz spectrometer. This power is split between the emitter and detector arms of our setup and after losses in the optical elements between the laser output and the antennas, each beam's power is reduced to 35 mW. Ideally, we would operate the antennas in the saturated regime (greater than 165 mW of fluence [34]) so that laser power fluctuations would not lead to terahertz amplitude fluctuations.

1.2.2 Laser optics

Figure 1.5 illustrates the array of optical elements that sits between the output of the Ti:Sapph oscillator and the antennas. The laser beam is first expanded by a pair of lenses to fill the full aperture of objective lenses situated near the antennas. To compensate for the dispersion that the beam will experience through the ensuing optical elements, the beam is then reflected back-and-forth between a pair of negative-dispersion chirp mirrors. Each mirror has a group delay dispersion of -60 fs^2 at 800 nm and the beam reflects back-and-forth 27 times (13 round trips, plus one more bounce).

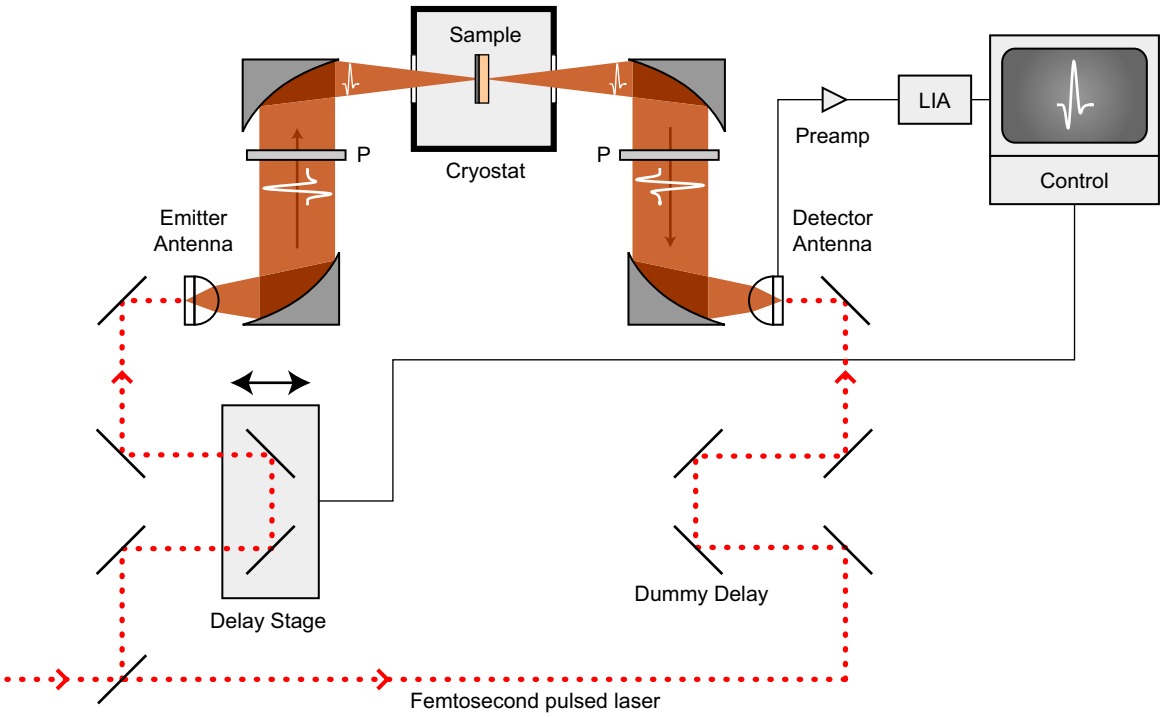

Figure 1.4: Full THz-TDS setup. A femtosecond pulsed laser is split into two arms: one for terahertz pulse emission and one for its detection. When a laser pulse strikes the emitter antenna, photocarriers are created and a terahertz pulse is emitted. The terahertz pulse is collected and focused into the cryostat by paraboloid mirrors and transmitted through our sample. Two more paraboloid mirrors collect and focus the terahertz pulse onto the detector antenna. Linear polarizers (P) sit in the collimated pulse paths. The detector antenna is gated by the femtosecond laser pulses; the picosecond-long terahertz pulses can thus be mapped in the time domain by varying the emitter arm path length with a computer-controlled delay stage. The detected signal is amplified by a preamplifier and lock-in amplifier (LIA) and the data is recorded onto a computer.

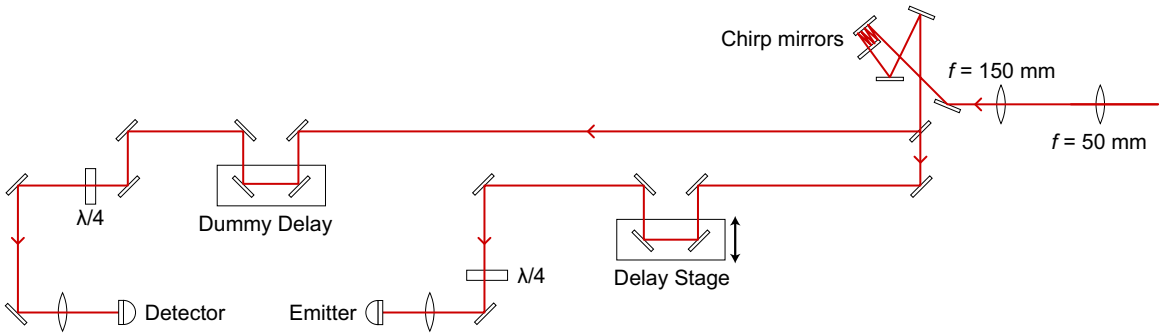

Figure 1.5: Schematic of our femtosecond laser optics. The beam enters from the right and is widened by two convex lenses. A pair of chirp mirrors induces negative dispersion in the pulses before the beam is split into the emitter and detector arms. The delay stage controls the relative arrival time of the emitter and detector pulses and the dummy delay compensates for the difference in path lengths of the two arms. Quarter wave plates ($\lambda/4$) prevent backreflections off the antennas from disturbing the Ti:Sapph mode-locking stability. Finally, the beams are focused onto the antennas.

The beam is then split into two arms: one for the stimulation of the emitter antenna and one to sample the response of the detector antenna. A computer-controlled delay stage is mounted in the emitter arm to vary the time between the stimulation of the emitter and detector; varying this time allows us to measure the terahertz pulse in the time domain. A second, "dummy" delay stage is mounted in the detector arm for coarse positioning of the terahertz pulse in the time-domain window of the delay stage. The beams in both arms then pass through objective lenses to focus the beams onto the antennas. Each objective lens is mounted on an XYZ stage for precise positioning and focusing of the beam onto the micron-sized antenna pad. The laser polarization is horizontal, so quarter wave plates near the antennas stop antenna backreflections from disturbing the mode-locked state of the laser.

Scattering lifetime measurements of metals often require precisions of a few femtoseconds. Consequently, the path length difference between the laser pulses (and thus the phase of the generated terahertz pulses) is stabilized by enclosing the laser optics in a box and controlling ambient temperature fluctuations to within 1°C. In practice, the temperature is often stabilized to within just 0.1°C. Furthermore, we limit the humidity fluctuations. While there are long-range drifts in relative humidity (RH) of up to 10% (i.e. from 20% to

30%), the RH is often stable for a few hours to within less than 0.1%.

1.2.3 Antenna fabrication

The antennas are fabricated in-house via an etching process and then sent for O^+ ion implantation at CORE Systems.[1] The ion implantation is heavy, rendering the silicon nearly amorphous and reducing the carrier trapping time τ_c to less than one picosecond [14]. This increases the high-frequency signal-to-noise (SNR) ratio in our system [11].

1.2.4 Antenna lenses

Sitting on the surface of the sapphire substrate, our antenna's radiation pattern is different from that of an antenna in free space. The terahertz pulses radiate preferentially into the sapphire side of the antenna, with a power ratio of n^3:1 between the substrate and air terahertz intensities [13], where n is the substrate index of refraction. This directionality is certainly advantageous for aiming the terahertz pulses towards our samples; however, the problem of coupling this substrate radiation into free space propagation remains. Hyperspherical lens are typically mounted against the sapphire substrate to facilitate this coupling and to partially collimate the terahertz beam. Previous antenna setups have used sapphire lenses to match the refractive index of the antenna substrates identically [23], but studies of high-resistivity silicon have shown it to have low power absorption and little variation in the refractive index from 0.2 to 2.0 THz, making it a superior choice [29].

A nearly aplanatic lens can be created from a sphere of radius R by simply lapping it down to the appropriate thickness, so long as the wavelength of the radiation is less than R [34]. We fashion our lenses out of spheres of radius $R = 5$ mm so that terahertz components above 60 GHz are faithfully emitted and detected. As illustrated in Figure 1.6, if the radius of the sphere is R and its index of refraction is n, then any incoming ray will be focused to a point F on an internal concentric sphere of radius R/n. The terahertz index of refraction of high-resistivity silicon is $n = 3.42$, so our dipole source or detector must be a distance

$$d = R\left(\frac{n+1}{n}\right) = 6.462 \text{ mm} \tag{1.2}$$

[1] http://www.coresystems.com/

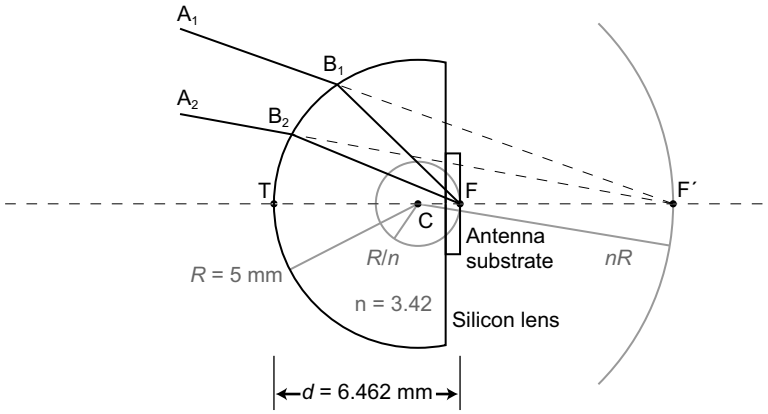

Figure 1.6: Antenna lens geometry. Rays AB that are directed towards a virtual focus F' can be aplanatically focused to a point F by a spherical lens. If the sphere is of radius R and refractive index n, then the center C of the lens is placed a distance nR from F' and the point F lies a distance R/n away from this center on the line CF'. Our spherical silicon lenses get machined so that the dipole antenna (etched on a substrate) sits at this point F, a distance $d = TF$ away from the front of the lens.

from the front of the lens. This lens geometry gives a numerical aperture of NA $= 1/n$, or a half-angle spread of 17°. The lens would be completely aplanatic if it weren't for the mismatch between the indices of refraction of silicon and our sapphire antenna substrates.

1.2.5 Terahertz focusing and polarization

The partially collimated terahertz beam is then focused by the paraboloid mirrors through the sample to a 1/e Gaussian beam diameter of 8 mm for 100 GHz frequency components (and less for higher frequencies) This diameter is diffraction limited at $d_0 \sim \frac{f/\#_{\text{eff}}\lambda}{\pi}$ for the focusing paraboloid mirror [48]; however, with mirrors of aperture size $f/0.145$ and a range of wavelengths between 0.3 and 3 mm, we do not approach this limit, despite careful alignments by myself and other students [34].

The configuration of paraboloid mirrors shown in Figure 1.4 inherently leads to beam clipping; I examine this behaviour in Figure 1.7. In two dimensions, a parabola with focal length f_p is defined by the curve $y = x^2/4f_p$. Simple geometry dictates that the effective focal length f_{eff} of the paraboloid mirrors shown is related to the focal length of the entire parabola by $f_{\text{eff}} = 2f_p$. Consider a collimated beam whose central ray strikes the first

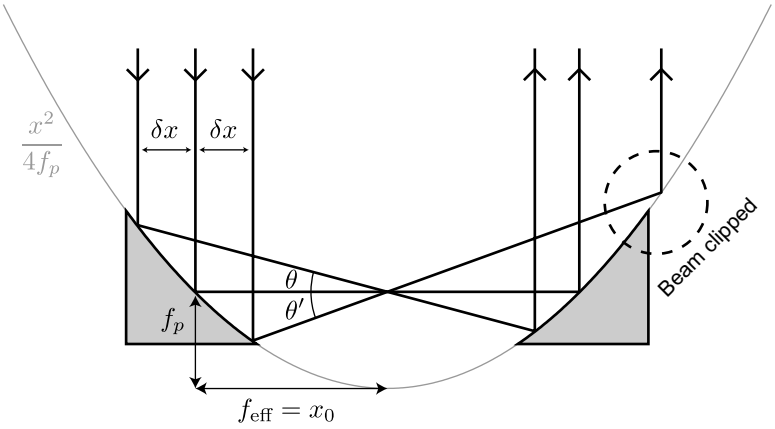

Figure 1.7: Beam clipping in the parabolic mirror arrangement. A collimated beam is focused such that the beam's central ray is reflected at 90°. The angles θ and θ' at which the outer rays approach the focus are not equal, so neither are their vertically opposite angles. Upon leaving the focus, the outer rays do not trace symmetrical paths to the rays entering the focus, and some of the beam does not hit the paraboloid mirror.

mirror and is reflected by 90° into the focus of the parabola; in particular, consider its outer rays. The curvature of the parabola reflects these parallel rays at different angles so that the angles θ and θ' formed between the outer rays and the central ray at the focus are not equal: $\theta' > \theta$. If the focused beam is collected by another paraboloid, the "top" ray leaves the focus with angle θ'. If θ is the maximum angle that a "top" beam can leave at from the focus, then this ray will not be collected by the mirror and the beam will be clipped. This can be avoided by rotating the collecting mirror by 180° about the central ray segment that passes through the focus, but this also increases the space requirements of the arrangement. We choose to tolerate some beam-clipping for the sake of a more compact setup.

It is often necessary to make directional measurements of our samples; to this end, we linearly polarize the terahertz pulses before and after they are transmitted through the sample. The location of the two wire-grid polarizers is shown in Figure 1.4.

1.2.6 Terahertz environment

Ambient humidity can be problematic, as water has absorption lines in the terahertz regime. The paraboloid mirrors and polarizers are enclosed in a box that is purged with nitrogen gas to avoid this absorption and limit whatever humidity fluctuations might remain in the

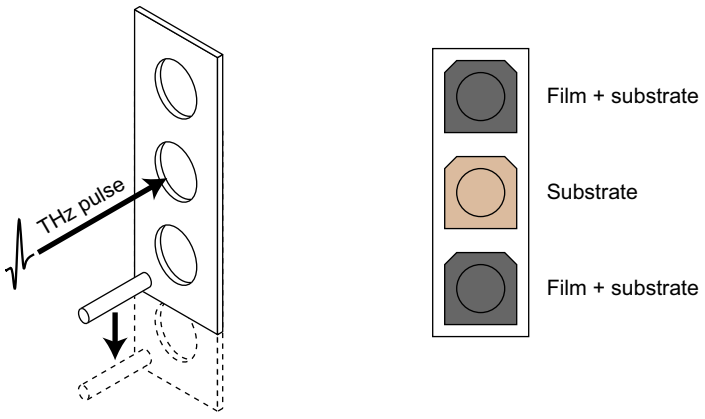

Figure 1.8: Sample positioning and mounting. Left: Our apertures move vertically as we take measurements on different specimens. Right: typical specimen mounting arrangement, with our reference specimen typically placed between the two samples of interest.

laboratory. The importance of the box is very visible when taking measurements with its top open; a ceiling vent near the terahertz beam causes wild path length fluctuations as the air conditioning turns on and off.

1.2.7 Sample environment and positioning

For low temperature measurements, our samples are mounted on a sample stick that moves vertically in a Janis Optical Systems STVP-100 continuous flow cryostat that can operate at liquid helium temperatures. The terahertz pulses enter and exit horizontally through two sets of Mylar windows: an inner "cold" set and an outer set at room temperature, separated by the cryostat vacuum jacket (four windows total). Vertical positioning of the sample stick is facilitated by a second set of quartz windows on the cryostat. These quartz windows are mounted orthogonally to the Mylar windows; that is, the pair of Mylar windows are mounted along the east-west axis and the quartz windows are mounted north-south.

The samples are mounted on apertures, like those shown in Figure 1.8. Our setup uses sets of three circular apertures that are either 8 mm or 12 mm in diameter (to accommodate 10×10 mm or 15×15 mm samples). These apertures are mounted on a sample stick and vertically positioned in the path of the focused terahertz pulses by a 4" MDC Vacuum Products Corporation drive shaft, a MicroKinetics stepper motor, and a MicroKinetics

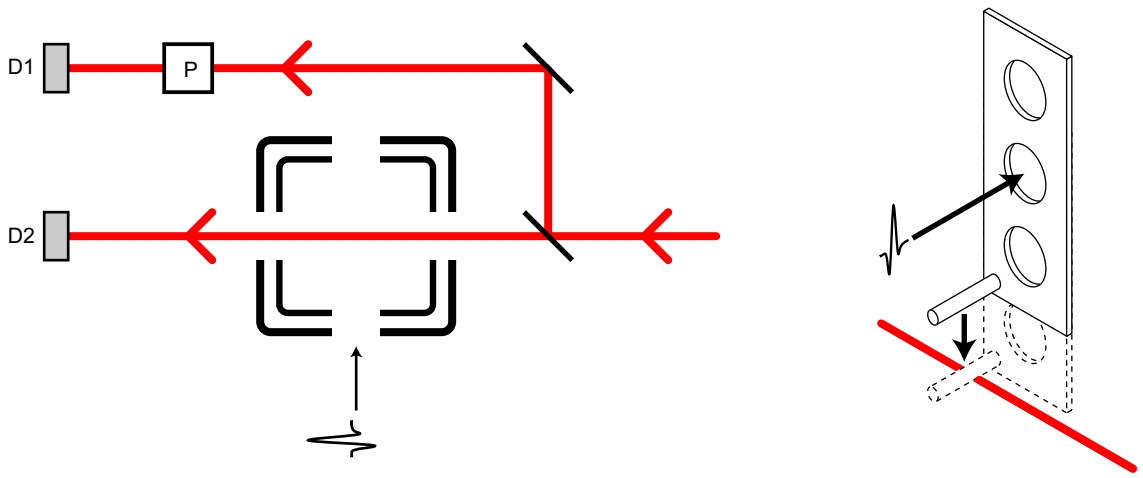

Figure 1.9: Nullfinding setup. Half of a diode laser beam passes through our cryostat, and half of it is directed around it. A polarizer P is adjusted so that the intensity of the outside beam is half that of the beam inside the cryostat. Photodetectors D1 and D2 measure the beam intensities. When the beam is half-blocked by the peg mounted on the apertures, the intensities of the two beams are equal and the null point is established.

MN100 motion controller. Typically in one "run" we make transmission measurements through the bottom, middle and top apertures consecutively before pulling the sample stick back out of the terahertz beam. At this point we may change an experimental parameter, like the cryostat temperature. We use rubber cement to mount the samples to the apertures because it continues to be adhesive at liquid helium temperatures. We remove the samples either by prying them off with a razor blade or by dissolving the rubber cement with methanol.

Incorrect vertical positioning of the apertures can lead to unwanted pulse distortion and scattering. We reference the aperture positions to a position determined by a small diode laser—a procedure we call "nullfinding". The nullfinding laser is split into two arms, as in Figure 1.9. One arm is directed through the cryostat orthogonally to the terahertz pulses and then strikes a photodiode upon its exit from the cryostat. The other arm is directed *around* the cryostat and strikes another photodiode after passing through a rotatable linear polarizer. We adjust the polarizer so that this beam that circumvents the cryostat is half the intensity of the beam that has passed through the cryostat. We also mount a small peg to the plane of the apertures. Subtracting the two photodiode signals, the difference is

therefore zero when the cryostat beam is half-blocked by the peg. With this zero value, we have found our "null" and a reference point from which we can we measure the distance of each aperture.

Transmission measurements through three different samples can be taken successively by simply moving the sample stick the appropriate distance so that the right aperture is in the path of the terahertz pulses. Typically, two of our samples are thin metal films on substrates and the third is a bare reference substrate. We then compare the transmissions through a film-on-substrate sample to the transmission through a bare substrate to isolate the response of the metal film. Mounting the reference substrate between the two films as in Figure 1.8 reduces systematic error from long-term drifts; if measurements are made from bottom to top, the time separations between the substrate measurements and the two film measurements are equal.

I have determined that mechanical hysteresis is important, so we avoid changing the sample stick direction of motion when either nullfinding or positioning the apertures. If the direction of motion must be changed (for example, when starting a new run), we take care to find the null again before making further measurements. Furthermore, the sample stick will certainly contract or expand over the large temperature range of our measurements (10–300 K), changing the null position, so we make sure to find the null again if we change the cryostat temperature.

1.2.8 Detection electronics

The terahertz pulses are detected by the same silicon-on-sapphire antennas that are used to produce them. The femtosecond laser again creates photocarriers in the antenna, but here, the incident terahertz pulse acts as the driving bias to the photocurrent. Hence, the photocurrent is a measure of the amplitude of the pulse at the time when the laser pulse is incident. By varying the time delay between the emitter and detector pulses, one can map out the amplitude of the terahertz pulses in the time domain. This gated detection scheme is demonstrated in Figure 1.10. The laser pulses arrive from the right at a repetition rate of 100 MHz and create photocarriers in the antenna. The terahertz pulses arrive from the left at an identical repetition rate, as they are generated by a different arm of the same laser. The laser pulse duration is much shorter than that of the terahertz pulse, so instantaneous 'snapshots' of the applied bias across the antenna are taken. The delay stage of the THz-TDS setup (shown in Figure 1.4) controls the relative arrival time of the terahertz and laser

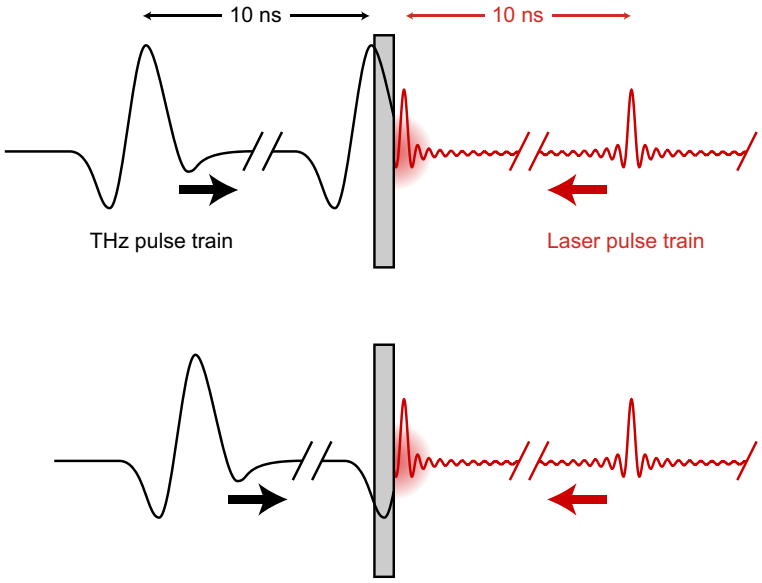

Figure 1.10: Gated detection in THz-TDS. Both laser and terahertz pulses arrive at the antennas at the same repetition rate and the short duration laser pulses serve to take 'snapshots' of the terahertz pulse (laser pulse width exaggerated in figure). We vary the delay between laser and terahertz pulses to sample the terahertz pulse in the time domain. Two detected points are shown in the top and bottom illustrations.

pulses so that the terahertz pulse is sampled in the time domain.

The detected photocurrent is amplified by a combination of a Femto LCA-100k-50m ultra-low-noise current preamplifier and a lock-in amplifier (LIA). The LIA is locked in to a 5 kHz, 3.5 V RMS sinusoidal bias applied to the emitter antenna. Compared to the ultrafast timescales of the antenna and laser, the bias is effectively dc. The measured signal is finally recorded from the LIA by a desktop computer.

1.3 Terahertz pulse characterization

A terahertz pulse is shown in Figure 1.11 in both the time and frequency domain. When measuring the pulses, we typically choose 256 delay stage positions i and collect the time position vector t_i and the pulse amplitude vector E_i. The $\{t_i\}$ are usually spaced by 0.1 picoseconds. The pulse's dc amplitude is unimportant, so we subtract it off and then condition the pulse with a Tukey (tapered cosine) window. A fast Fourier transform (FFT)

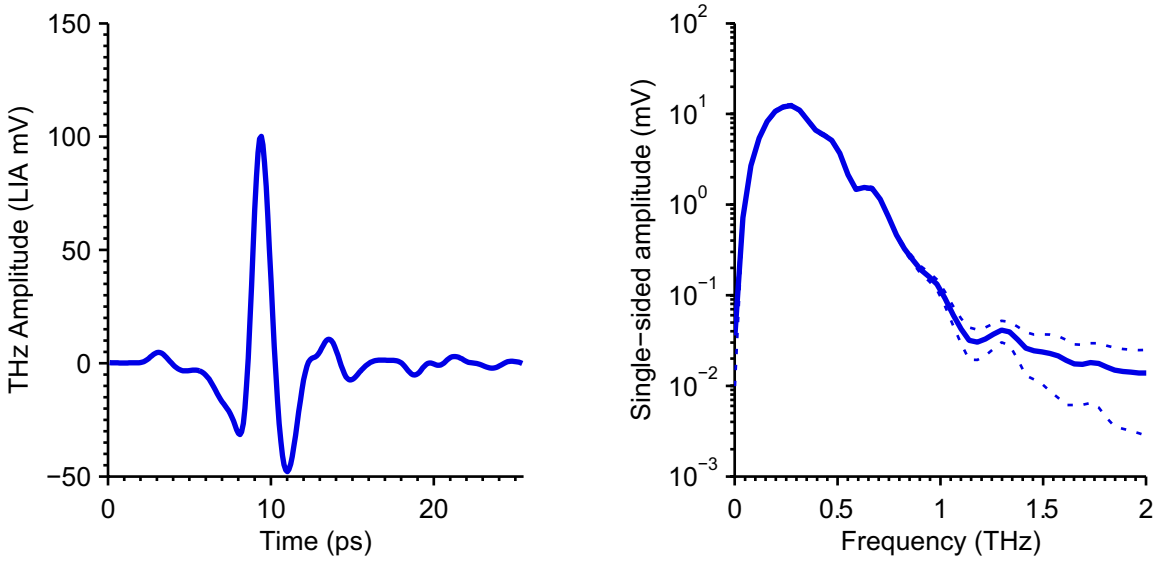

Figure 1.11: A typical terahertz pulse in the time domain (left) and frequency domain (right). The vertical axes are in units of millivolts, corresponding to our lock-in amplifier readout. The 1σ uncertainty envelope is not shown in the time trace, but can be seen as dotted lines in the frequency domain.

gives us frequency-domain Fourier coefficients $\tilde{E}_i$ at frequencies ω_i. We also define $E(t_i) \equiv E_i$, $\tilde{E}(\omega_i) \equiv \tilde{E}_i$ and the ideal, unmeasured pulse $\mathcal{E}(t)$ whose Fourier transform is $\tilde{\mathcal{E}}(\omega)$.

Sampling a THz pulse at this sampling frequency gives a Nyquist frequency of 5 THz, but the bandwidth over which reproducible measurements can be made is limited to 0.1–1.0 THz in our setup. At high frequencies, the pulse's spectrum decays exponentially; at the low end, the cutoff is partly due to the finite size of the silicon lens and partly due to decaying signal. Furthermore, the ion implantation that keeps the photocarrier lifetime short degrades with time, which in turn raises the noise floor and corrupts the high-frequency end of the bandwidth (the low-frequency end is steep enough that we don't see appreciable bandwidth degradation).

Chapter 2

Conductivity measurements with THz-TDS

The optical conductivity of a metal is a revealing window into its electronic structure. The Kubo formula for the conductivity demonstrates that peaks in the real part σ_1 of the conductivity represent collective excitations of a system, and redistributions of the spectral weight $S = \int_0^\infty \sigma_1 d\omega$ can indicate the influence of electron correlations. Measurements at microwave, infrared, and visible frequencies have yielded universal insights into the band structure and correlation effects in unconventional metals and superconductors. Our goal is to measure the optical conductivity in the terahertz regime.

2.1 Optical conductivity and the extended Drude model

The Drude model describes the optical conductivity of free carriers in conventional metals. The model assumes a single scattering mechanism with a collision rate of $\gamma = 1/\tau$, which yields an optical conductivity of

$$\tilde{\sigma}(\omega) = \frac{\sigma_0}{1 - i\omega\tau}, \tag{2.1}$$

where σ_0 is the dc conductivity. To describe metals with more complicated spectra, the extended Drude model [4] is often used. In it, the scattering rate is transformed to be frequency-dependent and complex, $\gamma \to \gamma(\omega) - i\omega\lambda(\omega)$, so that the optical conductivity is

modeled by

$$\tilde{\sigma}(\omega) = \frac{\epsilon_0 \omega_p^2}{\gamma(\omega) - i\omega[1 + \lambda(\omega)]}. \tag{2.2}$$

Here, I have introduced the plasma frequency ω_p, which in the simple Drude model is related to the dc conductivity by $\epsilon_0 \omega_p^2 \tau = \sigma_0$.

Part of the appeal of the extended Drude model is that by defining an effective scattering rate $1/\tau' = 1/\tau[1 + \lambda(\omega)]$ and plasma frequency $\omega_p'^2 = \omega_p^2/[1 + \lambda(\omega)]$, Equation (2.2) returns to the form of the simple Drude formula. Under a specific set of assumptions, the terms $\gamma(\omega)$ and $\lambda(\omega)$ can be interpreted as the frequency-dependent momentum scattering rates and optical mass renormalization [4]. More specifically, $1+\lambda(\omega)$ is related to the renormalization of the Fermi velocity caused by electron correlations. The spectroscopic frequency range of THz-TDS is low enough to effectively determine constraints on the low-frequency values of $\gamma(\omega)$ and $\lambda(\omega)$ such that in this range, we can indeed make these interpretations [28]. The study of heavy fermion systems has also provided evidence that $1 + \lambda(\omega)$ can be interpreted as the mass renormalization under the assumption that the interactions are local: there is consistency between this optical mass renormalization and the renormalization measured in heat capacity measurements [12, 17].

In our low-frequency bandwidth, we define an effective scattering lifetime $\tau^* \equiv \tau[1+\lambda(0)]$ and plasma frequency $\omega_p^{*2} = \omega_p^2/[1 + \lambda(0)]$. This τ^* relates to the dc conductivity σ_0 and imaginary conductivity σ_2 by $\sigma_0 \tau^* = (d\sigma_2/d\omega)|_{\omega \to 0}$, and by virtue of Kramers-Kronig relations [30],

$$\tau^* = \frac{2}{\pi} \int_0^\infty \frac{1 - \sigma_1(\omega')/\sigma_0}{\omega'^2} d\omega'. \tag{2.3}$$

Hence, the effective parameter τ^* relates to an integral of the curvature of σ_1.

2.2 Principles of terahertz transmission

To extract material parameters like the optical conductivity with terahertz time-domain spectroscopy, we make transmission measurements through two specimens: a sample of interest and a reference specimen whose terahertz transmission properties are known. In the frequency domain, the sample and reference pulses are $\tilde{E}_2$ and $\tilde{E}_1$, respectively. For a thin metal film on a substrate, the reference is a second, bare substrate; for a bare substrate,

the reference is an empty aperture. In this section, I examine the information that can be extracted from the relative transmission of the two pulses..

2.2.1 The transmission quotient

The terahertz pulse data is collected in the time domain, but we typically want to measure the frequency-domain optical conductivity. As a last step before we begin extracting material parameters from our data, we fast Fourier transform (FFT) the pulses into a set of Fourier coefficients $\tilde{E}_{1,i}$ and $\tilde{E}_{2,i}$. The measure used in THz-TDS to characterize both substrates and films is the frequency-domain transmission quotient $\tilde{E}_2(\omega)/\tilde{E}_1(\omega)$.

The convolution theorem shows that we can divide out two measurements to isolate the response of the sample. The transmission of terahertz radiation through thin metal films and substrates is a linear time-invariant system. Consequently, the time-domain output $y(t)$ is related to the time-domain input $x(t)$ and system response $h(t)$ via a convolution:

$$y(t) = h(t) \otimes x(t) \equiv \int_{-\infty}^{\infty} h(t-\tau)x(\tau)d\tau = \int_{-\infty}^{t} h(t-\tau)x(\tau)d\tau. \tag{2.4}$$

By the convolution theorem, the frequency-domain output is simply the product of the input $X(\omega) \equiv \mathcal{F}[x(t)]$ and system response $H(\omega) \equiv \mathcal{F}[h(t)]$,

$$Y(\omega) = H(\omega)X(\omega). \tag{2.5}$$

Hence, if we make a measurement $Y_1(\omega) = H(\omega)X(\omega)$ of a system with frequency response $H(\omega)$ and measurement $Y_2(\omega) = G(\omega)H(\omega)X(\omega)$ of a combined system, we can "divide out" the common response between two measurements to isolate the response $G(\omega)$:

$$G(\omega) = \frac{Y_2(\omega)}{Y_1(\omega)}. \tag{2.6}$$

In a coarse picture of our analysis methods for thin metal films, $G(\omega)H(\omega)$ would represent the transmission of a terahertz pulse through a metal film and its substrate, while $H(\omega)$ would represent the transmission through just the substrate.

2.2.2 Propagation through a dielectric substrate

Determining the conductivity of a metal film requires that we first characterize the substrate material upon which it is deposited. The relevant substrate parameters are its terahertz

index of refraction and its thickness, both of which can be extracted from a transmission comparison to an empty aperture.

The terahertz pulses can be considered to be a sum of plane waves of the form $\mathcal{E}_\omega(t) = \mathcal{E}_0 \mathrm{e}^{i(kz-\omega t)}$. A plane wave of angular frequency ω propagating in a dielectric of complex refractive index $\tilde{n}(\omega)$ through a distance d is modulated by the propagation coefficient $P(\omega, d)$, where

$$P(\omega, d) = \exp\left(i\frac{\tilde{n}(\omega)\omega d}{c}\right) = \exp\left(i\frac{n(\omega)\omega d}{c}\right)\exp(-\kappa d). \tag{2.7}$$

Here, the complex refractive index is $\tilde{n}(\omega) = n(\omega) + in_i(\omega)$ and the extinction coefficient is $\kappa = \frac{n_i(\omega)\omega}{c}$.

Plane waves striking an interface between two dielectrics undergo transmission and reflection according to the Fresnel equations. When the radiation is at normal incidence the equations are greatly simplified, and for a dielectric with little absorption, the imaginary part n_i of the material's refractive index can be ignored. The field transmission coefficient for a wave passing from material 1 to material 2 is therefore

$$t_{1,2}(\omega) = \frac{2n_1}{n_1 + n_2}. \tag{2.8}$$

Similarly, the field reflection coefficient is

$$r_{1,2}(\omega) = \frac{n_2 - n_1}{n_1 + n_2}. \tag{2.9}$$

In THz-TDS, we compare the Fourier transforms of two time-domain pulses via the quotient $T(\omega) = \tilde{E}_{\mathrm{sample}}(\omega)/\tilde{E}_{\mathrm{ref}}(\omega)$. The full transmission through the substrate or through air is simply the product of the Fresnel transmission coefficients and the propagation coefficient; knowing how the two pulses should propagate and cross interfaces between media, we can find relationships between this transmission quotient and the optical constants of the sample in question [34]. The field amplitude transmission and the substrate index of refraction n_s are related by:

$$T(\omega) = \frac{4n_\mathrm{s}}{(1+n_\mathrm{s})^2}\exp\underbrace{\left[\frac{i\omega d}{c}(n_\mathrm{s}-1)\right]}_{\equiv i\phi} \tag{2.10}$$

Hence, if the substrate's thickness d is known, one can determine its index of refraction from the phase slope $\eta \equiv -\frac{d\phi}{d\omega}$ of the transfer function via $n_\mathrm{s} = -\frac{c}{d}\eta + 1$. Conversely, if the index

of refraction is known, one can determine the thickness of the substrate (or the difference in thicknesses between two substrates). One can also make simultaneous measurements of both n_s and d from the phase alone with a large enough time window [18]. The terahertz pulse will undergo partial internal reflections at the front and back surfaces of the substrate and a second, attenuated pulse will emerge from the substrate at a time $2n_s d/c$ later, giving a second, independent measure of the product $n_s d$. However, our time-domain window is typically not large enough to catch this second pulse.

2.2.3 Propagation through a thin film on substrate

Terahertz pulse transmission through a thin metal film can be solved by analyzing the electromagnetic boundary conditions at the air-metal and metal-substrate interfaces. The amplitude of the field decays exponentially in the film with thickness. However, when considering propagation in very thin films, the transmission equations are simplified by the fact that the film thicknesses are significantly smaller than their terahertz skin depths. Hence, we can replace the usual exponential amplitude decay with a linear decay, which allows us to consider only the average field amplitude, located at mid-depth in the film. Consideration of the boundary conditions on the electric and magnetic fields on both sides of the film leads to a relation between the field transmission and the film's complex conductivity [43], often known as the Tinkham formula:

$$\tilde{\sigma}(\omega) = \frac{n_s + 1}{Z_0 d_\mathrm{f}} \left(\frac{1}{T(\omega)} - 1 \right). \tag{2.11}$$

Here, n_s is the substrate's terahertz index of refraction, Z_0 is the impedance of free space and d_f is the film thickness.

We can rearrange the Tinkham formula to express $T(\omega)$ in terms of $\tilde{\sigma}(\omega)$ and model the conductivity with an extended Drude peak of the form

$$\tilde{\sigma}(\omega) = \frac{\sigma_0}{1 - i\omega\tau^*} \tag{2.12}$$

with a low-frequency effective scattering lifetime τ^*. We can also define a scaling constant $\kappa \equiv \sigma_0 d_f Z_0/(n_\mathrm{s}+1)$. In our measurement bandwidth $\omega \ll 1/\tau^*$, so this transmission model is faithfully approximated by

$$T(\omega) = \frac{1}{1+\kappa} \exp\left[-i\omega\tau^* \frac{\kappa}{1+\kappa} \right]. \tag{2.13}$$

We can see that broadly, it is the dc conductivity of a metal that attenuates a terahertz pulse and the scattering lifetime that phase shifts it.

2.3 Transfer function fits

We calculate the Fourier coefficients $\tilde{E}_{2,i}$ and $\tilde{E}_{1,i}$ of the sample and reference pulses, respectively. To extract a sample's optical constants, we fit a transfer function $T_{2,1}(\boldsymbol{\theta};\omega)$ to their quotient $\tilde{E}_{2,i}/\tilde{E}_{1,i}$, that is parameterized by the vector $\boldsymbol{\theta}$. A maximum-likelihood method determines a fit parameter estimator $\hat{\boldsymbol{\theta}}$. Both the input and output signals $\tilde{E}_{1,i}$ and $\tilde{E}_{2,i}$ carry noise with frequency-independent variances σ_1 and σ_2 and the direct quotient can amplify this noise when $\tilde{E}_1$ is small. Thus, rather than minimizing the conventional chi-squared function $\chi^2 = \sum_i \frac{1}{\sigma_i^2}|T_{2,1}(\boldsymbol{\theta};\omega_i) - \tilde{E}_2(\omega_i)/\tilde{E}_1(\omega_i)|$, we minimize the cost function [28]

$$C(\boldsymbol{\theta}) = \frac{1}{2}\sum_i \frac{|\tilde{E}_{2,i} - T_{2,1}(\boldsymbol{\theta};\omega_i)\tilde{E}_{1,i}|^2}{\sigma_2^2 + |T_{2,1}(\boldsymbol{\theta};\omega_i)|^2\sigma_1^2}. \tag{2.14}$$

As mentioned in Section 1.3, our terahertz pulses are typically oversampled in the time domain. We can therefore use the high-frequency part of our transformed spectra to estimate the noise variances $\sigma_{(1,2)}$. We call this fitting algorithm `fitrationaldelay`.

Our transfer function is a quotient of polynomials of degrees M and N in the Laplace variable $s = i\omega$, modulated by a phase $-\eta s$:

$$T_{2,1}(s) = \frac{b_0 + b_1 s + b_2 s^2 + \ldots + b_N s^N}{a_0 + a_1 s + a_2 s^2 + \ldots + a_M s^M} \mathrm{e}^{-\eta s}. \tag{2.15}$$

The parameter vector $\boldsymbol{\theta}$ therefore consists of η, the $\{a_j\}$ and the $\{b_k\}$. By choosing which of the variables $\{a_j\}$, $\{b_k\}$, and η are free fit parameters, this fit function is versatile enough to describe both the lossless propagation through our dielectric substrates and the conductivity of our thin metal films. We refer to a transfer function with polynomials of degree M and N as an (M, N) model. Two of the more common examples of this are the $(0, 0)$ model and $(1, 1)$, whose utilities are detailed below.

2.3.1 Parameter extraction

Determining the conductivity of a thin metal film on a substrate is a three-step process, outlined here.

1. The terahertz index of refraction of the substrate must be determined. Pulse E_1 is transmitted through an empty aperture and pulse E_2 is transmitted through the substrate. Either the sample substrate (upon which the film will be deposited) or reference substrate (which will be left bare) can be used here.

2. The difference in thicknesses between the sample substrate and the reference substrate is found. Pulse E_1 is taken through the reference substrate and E_2 is taken through the sample substrate.

3. The film is deposited on the sample substrate. Transmission measurements are taken; pulse E_1 passes through the reference substrate and E_2 passes through the film-substrate composite.

I describe the procedure for each of these steps below.

Finding the substrate index of refraction

The transmission quotient through a dielectric substrate (Equation 2.10) can be written more compactly as $T(\omega) = b_0 \mathrm{e}^{-\eta s}$. This motivates the use of a transfer function that has no frequency dependence in the amplitude, that is, a $(0, 0)$ model:

$$T_{2,1}(s) = \frac{b_0}{a_0} \mathrm{e}^{-\eta s}. \tag{2.16}$$

We also fix $a_0 = 1$, because including both b_0 and a_0 as fitting parameters is redundant. We often already know the thickness of a substrate to within 5%, so we use the parameter η to find the substrate's terahertz index of refraction. In this case, our reference pulse E_1 is through air and our measurement pulse E_2 is through the substrate. By comparison with Equation 2.10, we see that $n_\mathrm{s} = -\frac{c}{d}\eta + 1$.

Finding the thickness mismatch between substrates

If the reference substrate and sample substrate were identical, then the transfer function $T_{2,1}(s)$ would not need to be modulated by the phase factor $\mathrm{e}^{-\eta s}$ for measurements of thin metallic films. Indeed, the Tinkham formula is not modulated by any phase factor. However, the substrates are not the same; consequently, it is unlikely that they will have the same thickness to within the necessary precision (the metal's femtosecond scattering lifetime multiplied by the speed of light in the dielectric). This thickness difference would cause a phase change due to the difference in propagation coefficients of the two substrates (see Section 2.2.2).

If a thickness difference is being measured, then pulse E_1 is taken through the reference substrate and E_2 is taken through the sample substrate. Then, adjusting Equation 2.10

to account for the reference pulse being transmitted through a substrate instead of air, we have

$$T(\omega) = \exp\left[\frac{in_s\omega}{c}(d_2 - d_1)\right] = \exp(-\eta s) \tag{2.17}$$

Thus, the fit parameter η measures the thickness difference $(d_1 - d_2)n_s/c$. We can subtract away this thickness difference by modulating our metallic film transfer function by the fixed phase factor $e^{-\eta s}$. We refer to this phase slope η as the substrate mismatch.

Converting our transfer function to a Drude conductivity

Once the substrates are characterized, the film is deposited on the sample substrate. The transfer function $T_{2,1}$ between the film-substrate composite and the thickness-matched substrate is related to the dynamical conductivity by Equation 2.11, the Tinkham formula

$$\tilde{\sigma}(\omega) = \frac{n_s + 1}{Z_0 d_f}\left(\frac{1}{T_{2,1}} - 1\right),$$

where n_s is the refractive index of the substrate, Z_0 is the impedance of free space, and d_f is the thickness of the film. To describe Drude conductivity in a thin metal film, we use a $(1,1)$ model. Here, the reference pulse is taken through a thickness-matched substrate. The fact that the substrate is thickness-matched means that we can drop the phase factor $e^{-\eta s}$ in the transfer function because it has already be accounted for; we are left with

$$T_{2,1}(s) = \frac{b_0 + b_1 s}{a_0 + a_1 s} = \frac{1 - \tau s}{1 + \frac{Z_0 d}{n_s + 1}\sigma_0 - \tau s}, \tag{2.18}$$

where the second equality includes the Drude parameters of Equation 2.1. However, a $(1,1)$ model does not describe Drude transmission by itself; a second constraint, $a_1 = b_1$, is required. After imposing this constraint, we divide the numerator and denominator by $a_1 = b_1$, which again results in redundant fitting parameters. We therefore redefine our zero-order coefficients to $b_0/b_1 \to b_0$ and $a_0/a_1 \to a_0$, implying that Drude conductivity is described by

$$\tilde{\sigma} = \frac{n_s + 1}{Z_0 d}\left(\frac{a_0 - b_0}{b_0 + i\omega}\right). \tag{2.19}$$

Resistivity and scattering lifetime extraction

The resistivity ρ is easily determined as the $\omega \to 0$ limit of the (1,1) model Drude fit and the scattering lifetime τ is related to the conductivity by $\tau = \frac{1}{\sigma_0}\frac{d\sigma_2}{d\omega}\big|_{\omega\to 0}$. Hence we have

$$\rho = \frac{Z_0 d}{(n_s + 1)}\frac{b_0}{a_0 - b_0}, \qquad \tau = -\frac{1}{b_0}. \tag{2.20}$$

2.3.2 Substrate matching

The substrate mismatch is measured prior to film deposition. We start by repeatedly measuring η at room temperature using a (0,0) fit model. Room temperature measurements do not require the expensive use of liquid helium, so for substrates whose optical thicknesses is relatively independent of temperature (like $NdGaO_3$), we can take a large number of measurements that will almost suffice for low-temperature measurements. The phase slope at any temperature oscillates with an RMS amplitude of about 2.5 fs and with a period that seems to follow the laboratory air conditioning cycle (between 10 and 40 minutes), as can be seen in Figure 2.1. We believe this is due to the surface of the optical table expanding and contracting. By taking a large number of room temperature measurements, we can take a small number of low-temperature measurements and have an estimate of the uncertainty associated with each.

Not only does taking room temperature mismatch measurements provide the phase slope variance, but it also characterizes an 'anchor state' to which we should be able to return after any changes to the system. Experience has shown that the substrate mismatch before and after cooling down or remounting the samples can change by up to 10 fs; if this is the case, then the cause of this systematic error needs to be found. Often, it is simply a case of being more careful with the substrates: birefringent substrates need to be consistently oriented with respect to the polarized terahertz pulses and all substrates must be clean while taking measurements. The terahertz environment must also be in equilibrium, which requires that the terahertz box be closed. We often purge the terahertz box with nitrogen gas, which must also be considered when creating equilibrium conditions. The THz path length change due to this purging is 15–20 fs and the purging half-life is about one hour at 20 SLPM flow, so several hours must have passed since purging started. Chapter 4 investigates how measurements of η can be further refined.

We then cool the substrates down to measure the mismatch at the rest of our measurement temperatures and then repeat the room temperature measurements. For some

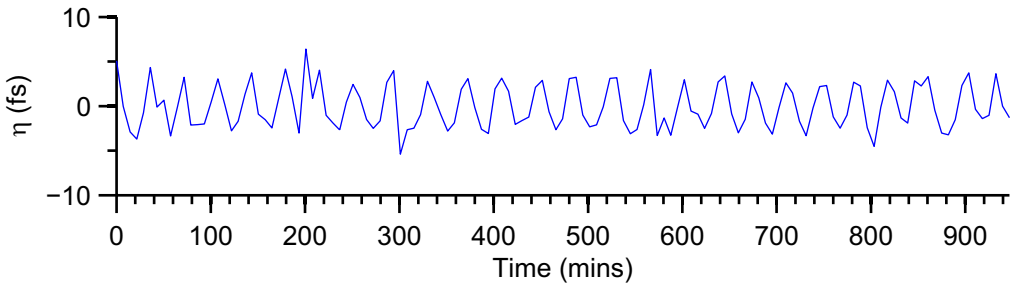

Figure 2.1: Phase slope η variation with time. Pairs of pulses were transmitted through a $NdGaO_3$ substrate, with the first pulse being the reference and the second being the 'sample'. The data has a trivial mean of zero, a standard deviation of 2.5 fs, and a period of roughly 40 minutes.

substrates like $NdGaO_3$, the mismatch will not significantly change at low temperatures and the expensive process of cooling the substrates can be significantly cut back. Once we have these measurements, the metallic films can then be deposited on the substrates.

2.4 Noise in our terahertz pulses

The noise in the terahertz pulses can be categorized into three types for the sake of analysis: multiplicative noise, time-domain "jitter", and additive noise.

The multiplicative noise can be broadly divided into "low-frequency" (LF) multiplicative noise, which affects the amplitude of each time-domain pulse uniformly, and "high-frequency" (HF) multiplicative noise, which affects each sampling point individually. Algebraically,

$$\text{LF multiplicative noise}: \qquad E_i \to \xi E_i \tag{2.21}$$

$$\text{HF multiplicative noise}: \qquad E_i \to \xi_i E_i, \tag{2.22}$$

with ξ being a single scalar and $\text{diag}(\xi_i)$ being a diagonal matrix. The parameters ξ and ξ_i are drawn from Gaussian distributions with mean value 1 and variances σ_ξ and σ_{ξ_i}. Similarly, one can define low- and high-frequency jitter: LF jitter results in a uniform phase shift of a terahertz pulse in the time domain, whereas HF jitter is caused by sampling the

pulse imprecisely in the time domain. Algebraically,

$$\text{LF jitter}: \qquad t_i \to t_i + \tau \tag{2.23}$$

$$\text{HF jitter}: \qquad t_i \to t_i + \tau_i, \tag{2.24}$$

with τ being a single scalar and τ_i being another vector of length 256. Again, τ and τ_i are drawn from Gaussian distributions with mean value 0 and variances σ_τ and σ_{τ_i}. Finally, we characterize point-wise additive noise by the transformation

$$\text{additive noise}: \qquad E_i \to E_i + \epsilon_i, \tag{2.25}$$

with ϵ_i being a vector with entries drawn from a Gaussian distribution of mean value 0 and variance σ_ϵ. Figure 2.2 represents these noise modes graphically. It turns out that both HF noise modes are insignificant, so all in all, the terahertz pulse $\mathcal{E}(t)$ is transformed to

$$E(t_i) = \xi\mathcal{E}(t_i + \tau) + \epsilon_i. \tag{2.26}$$

Having defined these five modes of pulse noise, we can characterize the impact of each of them on the variation of each sampling point's amplitude using a method developed by my colleague Payam Mousavi. The method compares the point-wise standard deviations of a large number of supposedly identical pulses to the point-wise standard deviations on artificially noisy pulses, generated from an "ideal" pulse.

We measure a fixed number of supposedly identical pulses, condition the pulses as per Section 1.3, and calculate the standard deviation σ_i in the amplitude at each sampling point (i.e 256 standard deviations for a 256 point pulse). This is one side of the comparison we are making. From this set of pulses, we can also determine the average times at which they were sampled $\bar{t}_i$ and the average amplitude at each sampling point $\overline{E}_i$ ("times" here refers to the independent variable in the time trace of Figure 1.11, not the times of day at which the measurements were taken). This set of average sample times and average amplitudes becomes our "ideal" pulse $\mathcal{E}(t)$.

We then take this ideal pulse and generate a large number of noisy pulses from it, with the noise determined by the strength of our fitting parameters σ_ξ, σ_{ξ_i}, σ_τ, σ_{τ_i}, and σ_ϵ. The point-wise standard deviation in these pulses is the other side of the comparison we are making. A least-squares fit of the noise of the generated pulses with respect to the noise of the measured pulses reveals the impact that each of the five fitting parameters have.

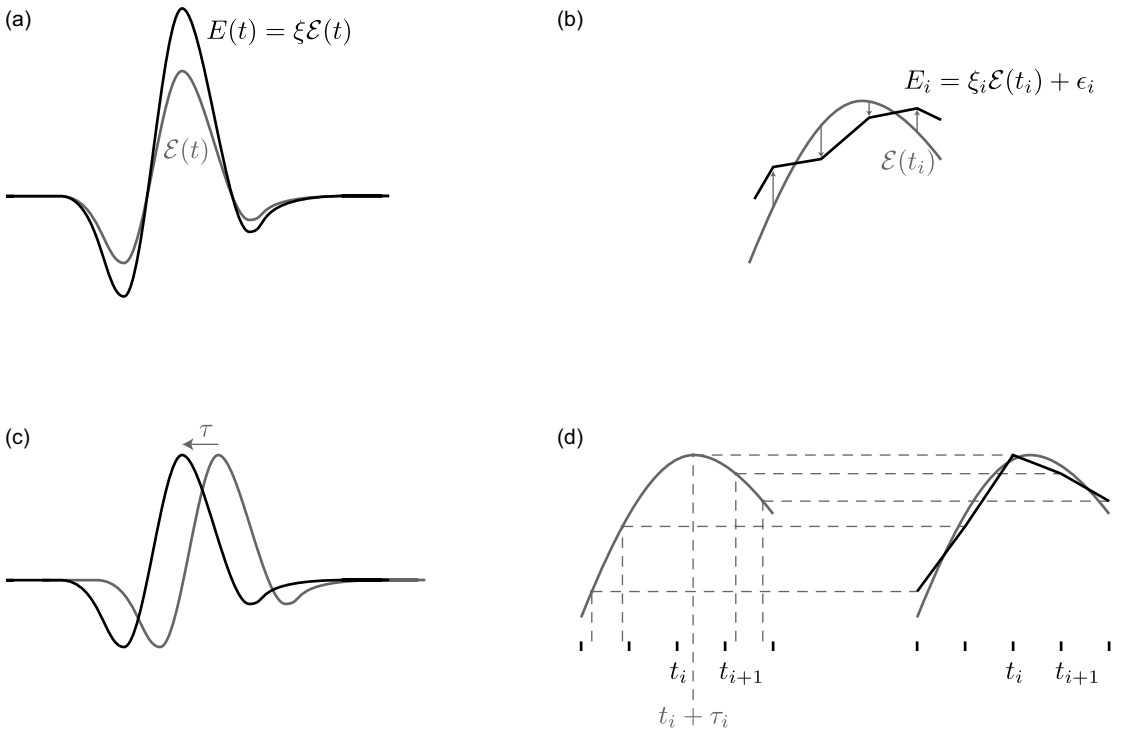

Figure 2.2: Noise modes in our terahertz pulse acquisition. Black and grey curves represent measured and ideal pulses, respectively. (a) Low frequency multiplicative noise, where the pulse is uniformly scaled by a factor ξ. (b) High frequency multiplicative noise and/or additive white noise, where each sampled amplitude E_i is individually scaled by a factor ξ_i and/or shifted by a value ϵ_i. (c) Low frequency measurement jitter, where the pulse phase is shifted by a time τ. (d) High frequency jitter. There is imprecision τ_i in the times at which the pulse is sampled (left), which results in inaccurate mapping of the measured amplitudes E_i to the times t_i (right).

This simulation shows that the LF multiplicative noise to scale as 0.8% of the THz amplitude, while the phase slope of each terahertz pulse has a standard deviation of 2 fs with respect to other pulses (LF jitter). The LF multiplicative noise roughly matches the laser power fluctuations and the characterization of the LF jitter is confirmed by the amplitude of the oscillating phase slope in Figure 2.1. The additive white noise contributes an amplitude variance of approximately 0.03 mV on a signal with 10–100 mV in maximum time-domain amplitude. I have also tried to measure the additive noise by blocking the emitter arm laser beam so that no THz signal is generated and then taking a time-domain trace of the detected noise. The RMS amplitude of this empty signal is 0.004 mV, independent of whether the lock-in amplifier's sensitivity is set to 20 mV, 50 mV, or 100 mV. The result from the simulation is larger than attempted direct measurements of the additive noise. J. F. Corson found in his thesis that the illumination of the antennas was the primary cause of the additive noise floor, outside of the Johnson noise limit [11]. There is likely additional additive noise carried by the THz pulse that we do not see when blocked the emitter arm laser; this may be the cause of the discrepancy between the noise floor simulations and measurements.

To measure the frequency-domain noise floor, I took the FFT of the measured noise signal (i.e. with the emitter arm blocked). The standard deviation of the Fourier coefficient amplitudes is 0.8 μV, which I take as the frequency-domain amplitude noise floor.

2.5 Constraints on samples

The Tinkham formula described in Section 2.2.3 puts constraints on the materials that can be studied with THz-TDS. Thick samples of highly conductive metals transmit very little terahertz radiation, with even less transmission at low temperatures. However, thinner samples are not always practical. The thinness is limited by the minimum film thickness that can be grown, as well as by the requirement that the thickness be greater than the mean free path of the carriers:

$$l = v_F \tau = \frac{\hbar}{\rho e^2} \left(\frac{3\pi^2}{n^2} \right)^{1/3}. \tag{2.27}$$

The mean free path at low temperatures must be considered here, which is significantly larger than the room temperature value. The resistivities ρ and carrier densities n of many elemental metals are widely available [1]; if the carrier density is not in the literature, it

can be estimated as $n = N_A Z \rho_m / A$, where N_A, Z, ρ_m, and A are Avogadro's Number, the electron valency, the mass density, and the molar mass, respectively. Where Z is difficult to determine, the estimate $Z = 1$ gives a minimum transmission estimate. Once an appropriate film thickness is determined, the single-sided transmission amplitude spectrum $|T(\omega)|$ of a metal film can be estimated by using Equation 2.11 with the Drude conductivity $\tilde{\sigma}(\omega) = \sigma_0/(1 - i\omega\tau)$ of the metal at the relevant temperature.

Much of the noise in our system is multiplicative (even the jitter scales with pulse amplitude, as it depends on dE/dt), so poor transmission is not a major obstacle to our measurements. Ultimately, it is the frequency-domain noise floor that limits the kind of samples we can measure; measurements at a frequency range of interest must be made with a sufficient signal to noise ratio.

Chapter 3

Transport anisotropy in calcium ruthenate

3.1 Introduction

Ruthenium oxides exhibit strong coupling between electronic, magnetic, structural, and chemical degrees of freedom; subtle changes in any of these parameters can lead to drastically different material properties. Calcium ruthenate $CaRuO_3$ is a paramagnetic metal [27, 9], whereas the substitution of strontium for calcium makes $SrRuO_3$ one of the rare 4d itinerant ferromagnets [45, 7, 36, 6]. Another member of the ruthenate family, Ca_2RuO_4, is a Mott insulator with antiferromagnetic ordering below 110 K [42] that can be rendered ferromagnetic with modest pressures [41]. For comparison, Sr_2RuO_4 is a superconductor that is isostructural with the superconducting cuprate $La_{2-x}Ba_xCuO_4$ [38]. Naturally, a great interest has arisen in such a diverse group of transition metal oxides.

The family's similarities to the cuprates can also be found in its members' infrared conductivity [33], mass renormalization [9], and deviations from standard Fermi liquid expectations [9, 31, 15]. However unlike the cuprates, neither $SrRuO_3$ nor $CaRuO_3$ is superconducting. We are thus able to study strong correlations and deviations from Fermi liquid theory in the low-temperature limit without the metallic properties being obscured by the onset of superconductivity.

Many properties of the ruthenates have been described well by density functional theory (DFT) [50, 46, 40], including the ferromagnetism of $SrRuO_3$, paramagnetism of $CaRuO_3$,

and antiferromagnetism of Sr_2YRuO_6 [5] (which can be thought of as an arrangement of alternating $SrRuO_3$ and $SrYO_3$ units in a lattice). However, strong renormalization of the plasma frequency ω_p from band theory predictions has been found in both $SrRuO_3$ and $CaRuO_3$, especially at low temperature [16, 30], and the mid-infrared conductivity of $CaRuO_3$ remains unexplained [35]. This would suggest the DFT picture of the ruthenium oxides is unsatisfactory.

An orthorhombic and distorted three-dimensional lattice [20] gives $CaRuO_3$ a strong anisotropy such that differences are expected in the *ab*-plane and *c*-axis conductivities. This thesis extends the research on $CaRuO_3$ by making directional conductivity measurements on thin films of this intriguing oxide metal.

3.2 Background

3.2.1 Crystal structure

Calcium ruthenate is the end member ($n \to \infty$) of a Ruddlesden-Popper series of the form $Ca_{n+1}Ru_nO_{3n+1}$ [10]. Here, n represents the number of neighbouring planes of RuO_6 octahedra, as can be seen in Figure 3.1. The compound exists in a *Pbnm* structure with an orthorhombic unit cell of dimensions $a = 5.36$ Å$, b = 5.54$ Å$, c = 7.68$ Å [44]. The pseudocubic lattice consists of corner-shared RuO_6 octahedra with the calcium cations fitting interstitially between the octahedra. Because of a size mismatch between the calcium cations and the lattice, the RuO_6 octahedra rotate in a perovskite distortion. This distortion occurs in several $ARuO_3$ materials (A = Sr, La, Ca, Pr), with the distortion increasing in the order of Sr, La, Ca, Pr [32]. The different ground states of ferromagnetic $SrRuO_3$ and paramagnetic $CaRuO_3$ are largely attributed to the different degrees of distortion in the two structures [35, 40, 49]. Indeed, DFT calculations of $CaRuO_3$ in the $SrRuO_3$ structure predict a ferromagnetic ground state.

3.2.2 Electronic structure

As an ionic solid, $CaRuO_3$ can be visualized as $Ru^{4+}(O^{2-})_6$ octahedra and electronically inert Ca cations. The ligand field splits the degeneracy between the ruthenium $4d$ e_g and t_{2g} orbitals such that the π-oriented t_{2g} shells sit 2 eV below the e_g shells. Hund's rule of maximum multiplicity is hence broken and the ruthenium is in a low-spin state. These

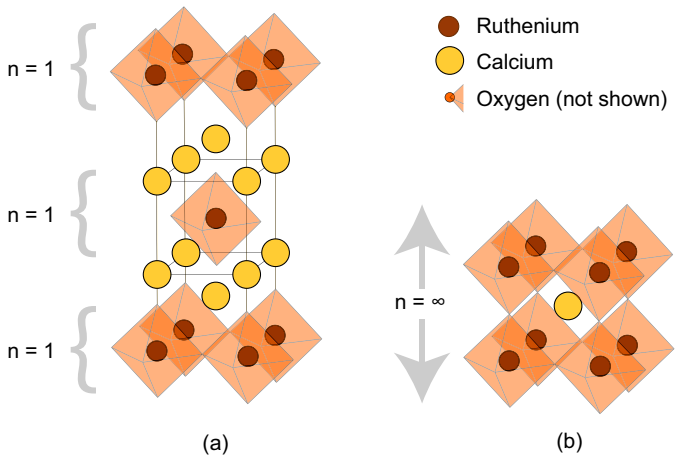

Figure 3.1: Ruthenium oxide structures: the $n = 1$ and $n \to \infty$ members of the Ruddlesden-Popper series $A_{n+1}Ru_nO_{3n+1}$. The index n is the number of connected planes of RuO_6 octahedra. Hence, structure (a) is highly two-dimensional and structure (b) is more three-dimensional. The structures shown are idealized; in both $SrRuO_3$ and $CaRuO_3$, the octahedra are rotated, distorting the lattice.

t_{2g} orbitals and the oxygen $2p$ orbitals with which the ruthenium shares π bonds are also hybridized and an electron from one of the three oxygens in the formula unit is transferred to the ruthenium atom, as demonstrated in Figure 3.2. This leaves 1/3 of a hole on each of these three oxygens.

In $SrRuO_3$, three of the Ru d bands are flat near the Fermi surface, leading to a sharply peaked density of states (DOS) near E_F [46]. This sharp peak implies that small changes to the location of E_F lead to large changes in the DOS, which may explain why a subtle change like the substitution of calcium for strontium can lead to a different magnetic ground state. The calcium ruthenate band structure is similar except that the flat bands are separated from each other. This leads to a doubly-peaked and reduced DOS near the Fermi surface, which may also reduce the tendency towards magnetism in this compound.

3.2.3 Conductivity spectrum of $CaRuO_3$

The infrared conductivity of $CaRuO_3$ is far from being conventional [35, 30]. Rather than having a single Drude peak at zero frequency, the real conductivity also has a broad finite-frequency maximum whose position scales with temperature above 100 K [35]. The question

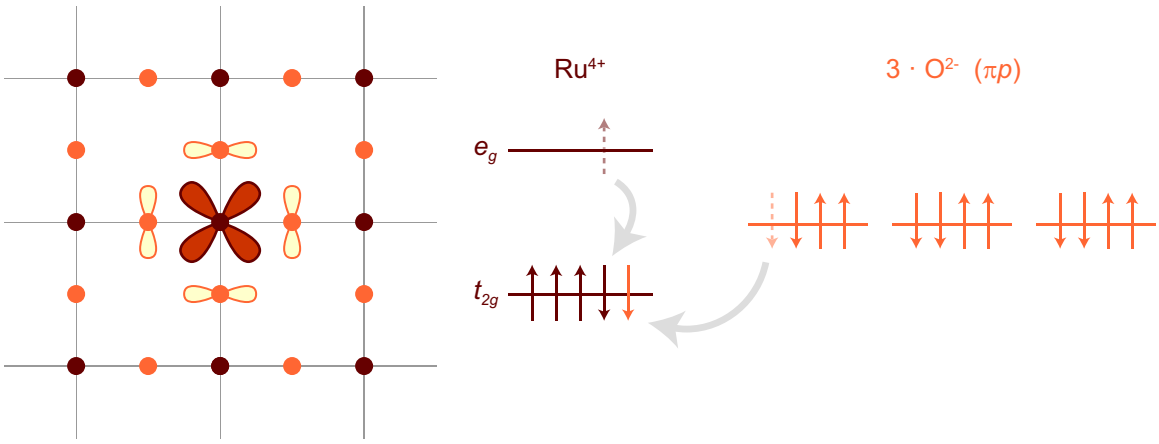

Figure 3.2: Electronic structure of $CaRuO_3$. The ruthenium atoms (brown) sit on an orthorhombic lattice and π-bond to the oxygen atoms (orange). The ruthenium is in a low-spin state and hybridization transfers an electron from one of the three oxygens in the formula unit to the ruthenium atom. Modified from Ref. [30].

of whether this maximum is due to an enhancement of finite-frequency conductivities or a reduced free carrier conductivity remains open. There is also evidence for significant redistribution of the partial spectral weight $S(\Omega) = \int_0^\Omega \sigma_1(\omega)d\omega$ in $CaRuO_3$ with temperature that is not explained by the Drude model.

Forced beyond the simple Drude conductivity model, we turn to the extended Drude model (Equation 2.2) to conduct our spectroscopic analysis:

$$\tilde{\sigma}(\omega) = \frac{\epsilon_0 \omega_p^2}{\gamma(\omega) - i\omega[1 + \lambda(\omega)]}.$$

This low-frequency approach has previously been used by Kamal *et al.* to describe the narrow Drude peak in $CaRuO_3$ that emerges at low temperatures [30]. One assumption of the extended Drude model is that there are no interband transitions in the system; with three bands crossing the Fermi level [40], $CaRuO_3$ may violate this condition. In spite of this, our use of the model remains valid in our low-frequency bandwidth [28].

3.2.4 Transport anisotropy

The distorted orthorhombic lattice of calcium ruthenate allows anisotropy in the conductivity of calcium ruthenate. The expected strength of this anisotropy is unclear, however.

Mazin and Singh predict a conductivity that is 50% stronger along the c-axis than in the ab-plane [40], but have conceded in a private communication that the calculation's convergence is weak and the predictions are delicate. Furthermore, the predictions are not reproduced in recent unpublished work that calculates plasma freqencies of $\omega_{p,ab} = 2.39$ eV and $\omega_{p,c} = 2.30$ eV [19]. There have also been experimental measurements of the resistivity anisotropy of $CaRuO_3$ [44, 47], but they contradict each other in the direction of the anisotropy. Kamal *et al.* have measured the ab-plane conductivity with THz-TDS [30] and have unpublished results that suggest little difference in the c-axis conductivity, but their precision is limited by uncertainty in the c-axis substrate mismatch, a crucial parameter in their determination of the transport properties. The current knowledge of transport anisotropy in calcium ruthenate seems uncertain at this point, so more study is clearly needed.

3.3 Experiment

3.3.1 Samples

Our samples are grown by the Oxide Laboratory at the University Wisconsin-Madison.[1] They are ∼50 nm films of $CaRuO_3$ deposited by 90° sputtering on Crystec low-miscut ($< 0.2°$) (110) $NdGaO_3$ (NGO) single-crystal substrates measuring 10 mm × 10 mm × 1 mm [21, 20, 25, 44]. The substrate is miscut in the $[\bar{1}10]$ in-plane direction of the substrates; this promotes single-domain growth of the film [25, 39, 44]. The film is grown such that the $[\bar{1}10]$ direction of the film is parallel to the $[\bar{1}10]$ direction of the substrate (Figure 3.3).

The samples are mounted in a liquid helium continuous flow cryostat and transmission measurements through both sample and reference are made at temperatures of 10–290 K. Because the terahertz pulse is linearly polarized before and after transmission through the sample, any anisotropy in the conductivity can be measured by simply rotating the sample, as in Figure 3.3.

[1] Department of Materials Science and Engineering, University of Wisconsin-Madison, Madison, Wisconsin 53706, USA.

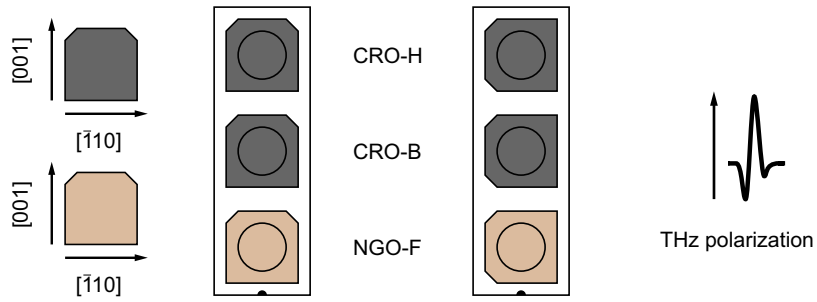

Figure 3.3: $CaRuO_3$ sample mounting: orientations for transport measurements along the c-axis (left) and in the ab-plane (right). $CaRuO_3$ films B and H were 55.1 and 53 nm thick, respectively. The advantages of mounting the reference substrate between the two films (as in Figure 1.8) had not been realized at the time of the experiment.

3.3.2 $NdGaO_3$ substrates

I measured the substrate thickness mismatch η of substrates NGO-B and NGO-H with respect to NGO-F. NGO is birefringent, so measurements must be made in both the ab-plane ($[\bar{1}10]$) and c-axis ($[001]$) directions. Figure 3.4 shows these measured mismatches for both pairs of substrates versus temperature for both orientations.

For substrates of physical thickness d and refractive index n, the optical thickness is $D = nd$. The logarithmic derivative yields

$$\frac{1}{D}\frac{\partial D}{\partial T} = \frac{1}{d}\frac{\partial d}{\partial T} + \frac{1}{n}\frac{\partial n}{\partial T}, \tag{3.1}$$

and if the change in D is small, then the factor $1/D$ can be moved freely in and out of any integrals, such as

$$\frac{\Delta D}{D} = \int_{T_0}^{T} \frac{1}{n}\frac{\partial n}{\partial T'}dT' + \int_{T_0}^{T} \frac{1}{d}\frac{\partial d}{\partial T'}dT'. \tag{3.2}$$

Both the index of refraction and thermal expansion of the physical thickness depend on the number of phonons in the system; hence both integrands relate to the temperature derivative of the Bose-Einstein distribution function:

$$\alpha = A\frac{\partial}{\partial T}\frac{1}{e^{B/T} - 1}. \tag{3.3}$$

Evaluating the integrals above and scaling the optical thickness D to a substrate mismatch

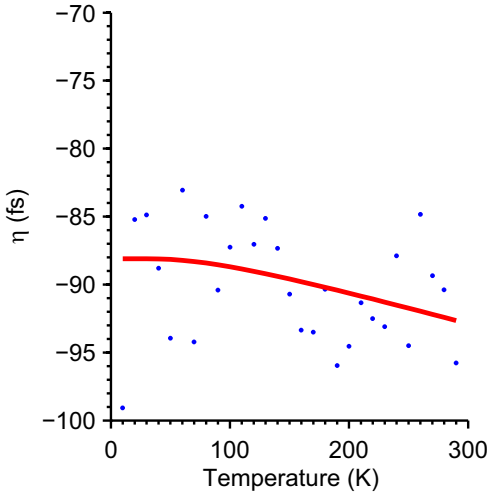

(a) Basal (*ab*-plane) substrate mismatch between NGO-B and NGO-F as a function of temperature. $A = -6 \pm 3$ fs, $\eta_0 = -93 \pm 1$ fs. $r = 1.3\sigma$.

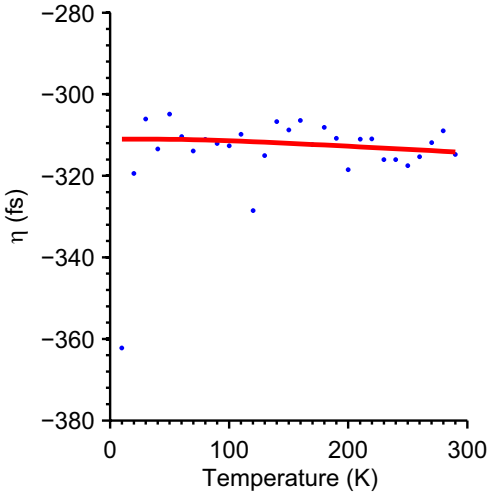

(b) Basal (*ab*-plane) substrate mismatch between NGO-H and NGO-F as a function of temperature. $A = -4 \pm 4$ fs, $\eta_0 = -314 \pm 2$ fs. $r = -0.20\sigma$.

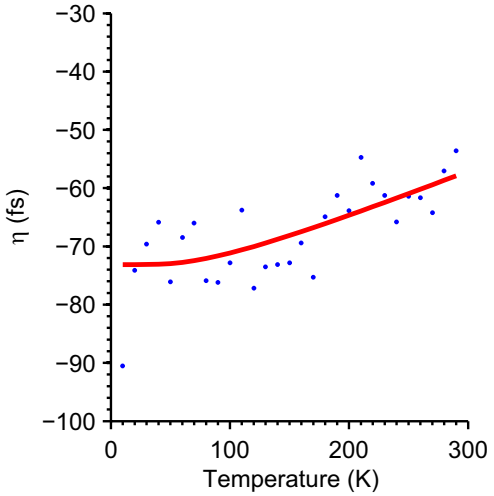

(c) Perpendicular (*c*-axis) substrate mismatch between NGO-B and NGO-F as a function of temperature. $A = 19 \pm 4$ fs, $\eta_0 = -58 \pm 2$ fs. $r = 2.6\sigma$.

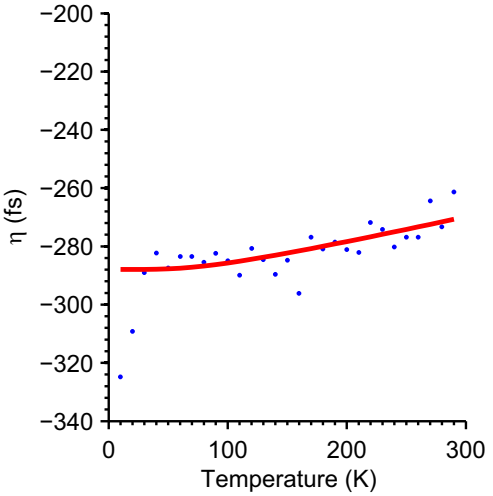

(d) Perpendicular (*c*-axis) substrate mismatch between NGO-H and NGO-F as a function of temperature. $A = 22 \pm 4$ fs, $\eta_0 = -270 \pm 2$ fs. $r = 0.58\sigma$.

Figure 3.4: Substrate mismatches η in the basal and perpendicular directions. Data fit to Equation 3.4 over the range 30–290K with $B = 238$ K and $T_0 = 290$ K.

η, we get

$$\eta(T) - \eta_0 = \frac{A}{\mathrm{e}^{B/T} - 1} - \frac{A}{\mathrm{e}^{B/T_0}}. \tag{3.4}$$

I fit this equation to the data in the range 30 K $\leq T \leq$ 290 K in Figure 3.4 with fixed parameters $B = 238$ K [34] and $T_0 = 290$ K. I then used this functional form for η in subsequent calculations.

Assuming this function fits the data well, the variance σ_η^2 of the fit residuals serves as a good measure of the noise in η. The covariance matrix of the fit parameters can therefore be calculated as $\mathbf{V}_{\boldsymbol{p}} = \frac{1}{\sigma_\eta^2}\tilde{\mathbf{G}}\mathbf{G}$, where $\mathbf{G}$ is the Jacobian of η with respect to the parameters $\boldsymbol{p} = (A, \eta_0)$. From this, we can see that the material parameter A is consistent between measurements in the same direction. In a single substrate, differences in η_0 are certainly expected between the *ab*-plane and *c*-axis measurements due to the birefringence of NGO. However, it is encouraging to see that for both substrates, η_0 is of the same order of magnitude between the two directions, given that the birefringence is not severe. Using the fit residuals to calculate σ_η^2 prevents us from using the χ^2 test to evaluate the goodness of fit, but the run test [3] confirms that the fits are good. Run test deviations r are listed in Figure 3.4 in units of standard deviations. The fit residuals have a standard deviation of approximately 5 fs, which is higher than the low-frequency jitter measured in Section 2.4 but not severely higher.

The parameter A describes the amplitude of the thickness change and should be proportional to the overall thickness. That is, if A describes the change in mismatch, it should be proportional to the full mismatch, and if A describes the change in the full thickness D of a substrate, $A \propto D$. This parameter was measured with B for a 1 mm substrate in Ref. [34] to have a value of $A = 272$ fs. Typical substrate mismatches are of the order 100 nm, so we expect that our values of A should be of the order 0.272 fs. We suspect that the large discrepancy might be due to expansion properties that are intrinsic to individual substrates, beyond the universal properties of $NdGaO_3$ single crystals. The fact that the mismatch increases at low temperatures for *c*-axis measurements is also strange. However, the point of fitting Equation 3.4 to the data is not so much to estimate the material parameters; rather, it is to find smoothly varying values of η with temperature that reflect the real data that we have taken.

Below 30 K, there is a potential for large statistical uncertainty that I address in Section

4.2, which is why I have omitted these points in the fit. I also took a large set of room temperature mismatch measurements, as I suggested was important in Section 2.3.2. However, there is a disagreement of roughly 10 fs between these measurements and the cooldown measurements, a disagreement which we believe is systematic. The cooldown measurements are more reproducible and were taken in experimental conditions that are closer to those of our conductivity measurements, so I have only used them in my subsequent analysis. Knowing the substrate mismatch in both directions allows us to make measurements of *ab*-plane and *c*-axis conductivity in $CaRuO_3$ and add to the work of Kamal *et al.*, who reported only *ab*-plane measurements [30].

3.3.3 Raw conductivity data

I present real and imaginary conductivity measurements of two films of $CaRuO_3$ (CRO-B and CRO-H) in Figures 3.5 and 3.6. Data at four temperatures ($T = 15, 50, 90, 290$ K) are shown in each plot, along with Drude fits from our `fitrationaldelay` fit algorithm. The data points are calculated using direct quotients of the terahertz transmission spectra $T(\omega) = \tilde{E}_{\text{sample}}(\omega)/\tilde{E}_{\text{ref}}(\omega)$ and the Tinkham formula (Equation 2.11), and the fits are restricted to the frequency range 250–800 GHz.

Kamal *et al.* have previously reported the emergence of a narrow Drude peak (with width ~ 1 THz) in $CaRuO_3$ at low temperatures in the *ab*-plane [30]. My data confirms this low-temperature behaviour in both the *ab*-plane and *c*-axis; however, the strength of the peak is weaker.

The peaks and valleys in the data points in the 0.5–1.0 THz range look suspiciously like systematic error or some kind of dissipation in the conductivity spectrum. In reality, we believe that they are actually the result of additive white noise in the time-domain pulses. This is supported by a numerical simulation. I start with a typical time-domain reference pulse $\mathcal{E}_1(t)$, which I shall call "noiseless" and therefore denote with the script $\mathcal{E}$. In this case, I have chosen a pulse that was measured through substrate NGO-F, oriented for *ab*-plane measurements and at a temperature of 50 K, but the details are not important. I define a second pulse $\mathcal{E}_2(t) \equiv \mathcal{E}_1(t)$ and then add white noise to each pulse to create "noisy" pulses $E_1(t)$ and $E_2(t)$. After conditioning the noisy pulses as in Section 1.3, I take their fast Fourier transforms and form the frequency-domain quotient $\tilde{E}_2/\tilde{E}_1$. Whereas the quotient of the "noiseless" pulses is unity at all frequencies (verified numerically), the noisy quotient has wiggles. One might hypothesize that these wiggles are merely statistical fluctuations

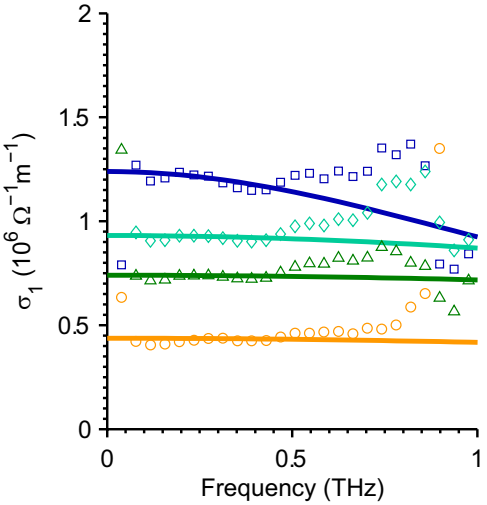

(a) Real part of the basal (*ab*-plane) conductivity in CRO-B.

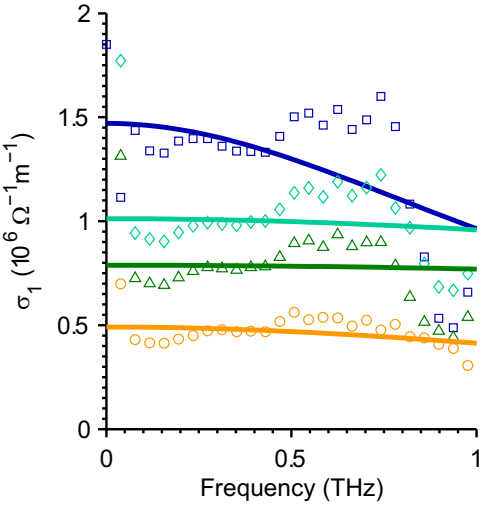

(b) Real part of the basal (*ab*-plane) conductivity in CRO-H.

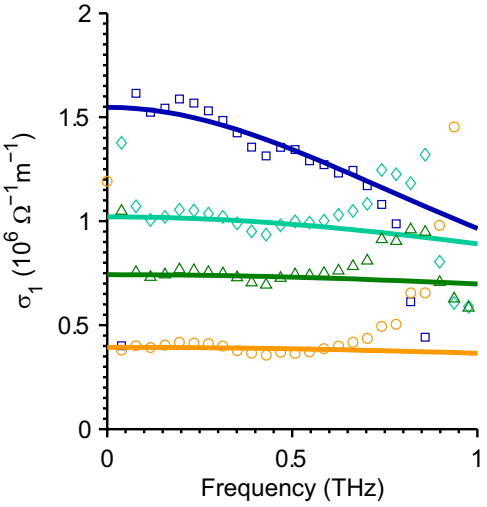

(c) Real part of the perpendicular (*c*-axis) conductivity in CRO-B.

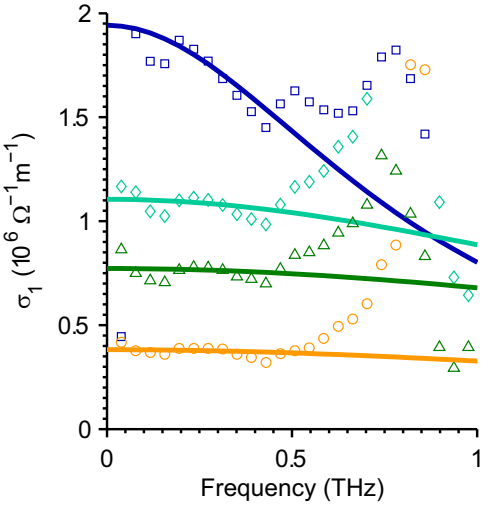

(d) Real part of the perpendicular (*c*-axis) conductivity in CRO-H.

Figure 3.5: Real conductivity vs. frequency in $CaRuO_3$ for temperatures $T = 15, 50, 90, 290$ K (top to bottom) in CRO-B and CRO-H. Open circles are data taken from direct transfer quotients; fits are Drude fits from `fitrationaldelay` transfer functions over the range 250–800 GHz.

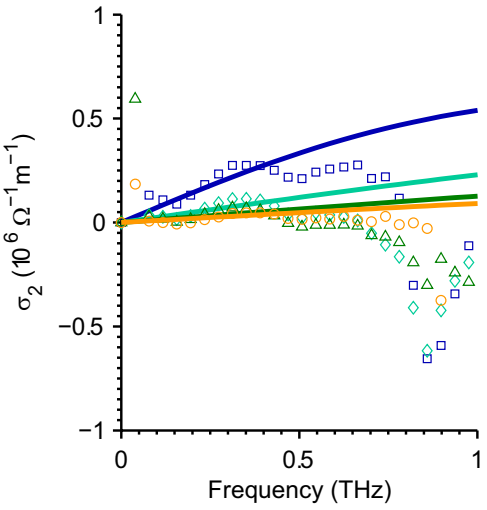

(a) Imaginary part of the basal (ab-plane) conductivity in CRO-B.

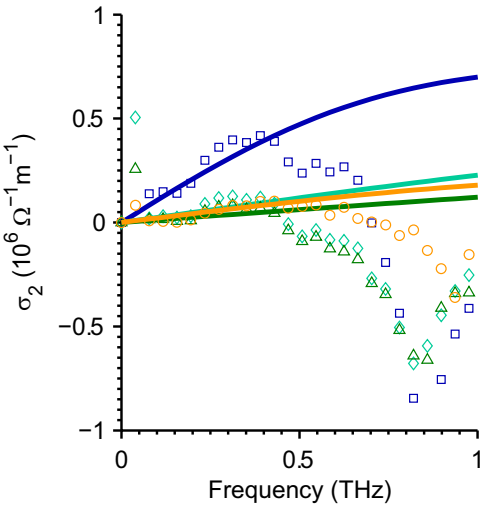

(b) Imaginary part of the basal (ab-plane) conductivity in CRO-H.

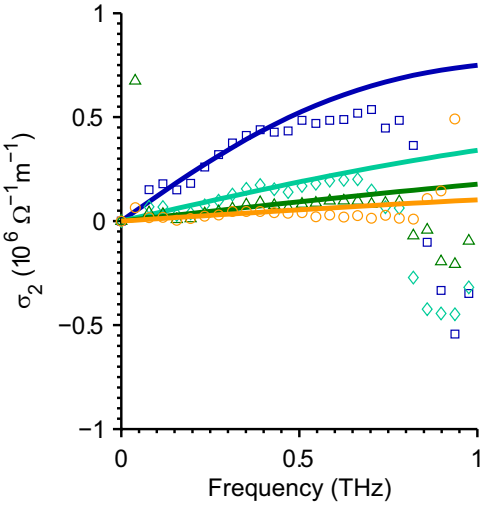

(c) Imaginary part of the perpendicular (c-axis) conductivity in CRO-B.

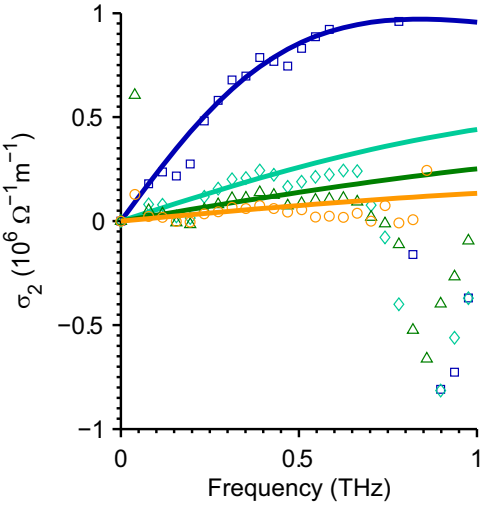

(d) Imaginary part of the perpendicular (c-axis) conductivity in CRO-H.

Figure 3.6: Imaginary conductivity vs. frequency in $CaRuO_3$ for temperatures $T = 15, 50, 90, 290$ K (top to bottom) in CRO-B and CRO-H. Open circles are data taken from direct transfer quotients; fits are Drude fits from `fitrationaldelay` transfer functions over the range 250–800 GHz.

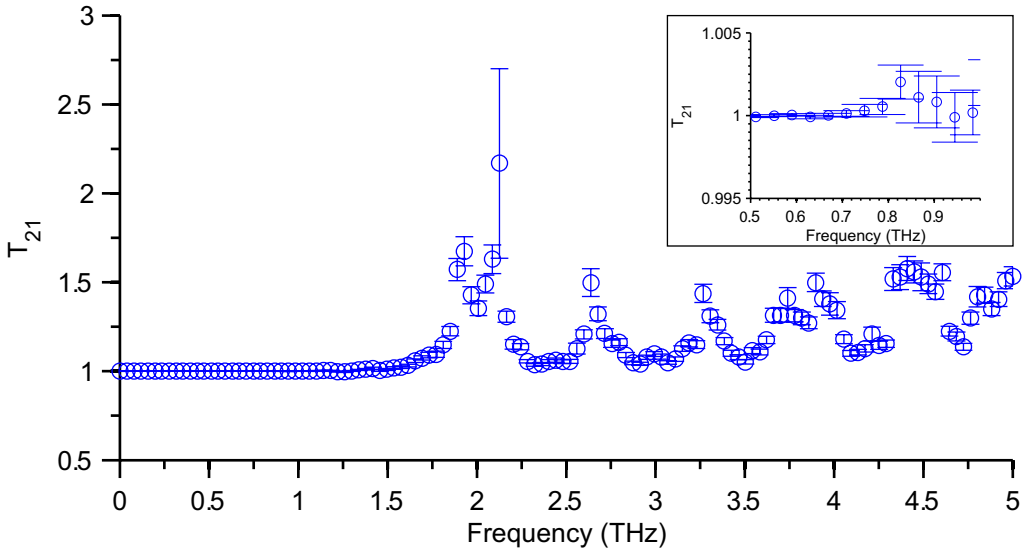

Figure 3.7: "Wiggles" in our transfer quotient. Time-domain additive noise in our terahertz pulse can lead to "wiggles" in the transfer quotient $T_{21} = \tilde{E}_2/\tilde{E}_1$. Noisy pulses E_1 and E_2 were generated 1000 times and their mean transfer function is plotted. The uncertainty in each mean is shown with the error bars, using the standard $\sigma/\sqrt{N}$ estimator. The additive noise had an standard deviation of 0.03 mV, as per the results in Section 2.4. The inset enlarges the region between 0.5 and 1.0 THz.

about unity; however, repeating this process 1000 times (with different white noise each time) and taking the mean transfer quotient yields the data in Figure 3.7. We can see that the transfer function wiggles are neither statistical anomalies nor resonances in the conductivity spectrum — they are merely artefacts of time-domain noise in the pulses that appear when the frequency-domain SNR is low.

We can try to emulate the wiggles in the conductivity data of Figure 3.5 using the time-domain additive noise measured in Section 2.4. Taking a real reference pulse from our measurements (like the one mentioned above), we can pass it through a frequency-domain transfer function with parameters that reflect the transport properties of a real CRO film, then transform this transferred pulse back to the time domain and add white noise to it. If we find the conductivity spectrum from this noisy transferred pulse and the original reference pulse, we should expect to see wiggles in the spectrum. Using additive noise with RMS amplitude 0.03 mV in this simulation, we do not fully reproduce the amplitude of the

wiggles in Figure 3.5. However, the wiggles are more faithfully reproduced with additive noise of amplitude 0.15 mV. Given that the phase slope noise in these measurements is higher than expected, perhaps it is not surprising that the additive noise may also be higher.

3.4 Discussion of results

A narrow Drude peak emerges in the conductivity of $CaRuO_3$ below 100 K. The width of this peak is measured by the effective low-frequency electron relaxation rate $\gamma^* = 1/\tau^*$, and its height is measured by the dc conductivity, whose reciprocal ρ is measured by our low-frequency effective Drude fits. From our Drude conductivity fits and the methods of Chapter 2, I extract the resistivity ρ and a low-frequency effective scattering lifetime $\tau^* = \tau[1+\lambda(0)]$.

Figure 3.8 shows that the residual resistivity of our samples is comparable to previous reports [44, 30]. The direction of the resistivity anisotropy between the *ab*-plane and *c*-axis is consistent with measurements by Schultz *et al.* [47], and contradicts measurements by Proffit *et al.* [44]; this is unexpected and further investigations should be done to confirm this. The crossover between the directional resistivities that Proffit *et al.* report is observed, but at $T \simeq 100$ K rather than $T \simeq 25$ K.

The effective scattering lifetime results in Figure 3.9 also demonstrate there is little anisotropy in τ^*. Consequently, there is little anisotropy in the product $\rho\tau^* \propto 1/\omega_p^{*2}$. As a matter of fact, the anisotropy in the system's plasma frequency seems to approach the more recent DFT predictions [19] at low temperatures as demonstrated in the inset to Figure 3.10. It is at low temperatures that we expect band theory predictions to hold best; these results provide evidence against which anisotropy calculations can be corroborated.

The quotient $(\omega_p/\omega_p^*)^2$ is a measure of the optical mass renormalization $1 + \lambda(0)$ in $CaRuO_3$. Consistent with *ab*-plane measurements by Kamal *et al.* [30], we see renormalization at all temperatures, and a sharp increase in the renormalization below 50 K (shown as an upturn in Figure 3.10) for measurements in both directions.

The full spectral weight of a Drude peak is characterized by ω_p^2, so the product $\rho\tau^* = 1/\omega_p^{*2}$ reveals changes in the spectral weight of our low-frequency Drude peaks. I plot this product versus temperature in Figure 3.10, along with band theory predictions. As shown previously by Kamal *et al.* [30], the sharp rise in the product at low temperature indicates that spectral weight is being shifted away from our terahertz frequency range as the system is cooled. At high temperatures, we expect renormalization to be temperature-independent;

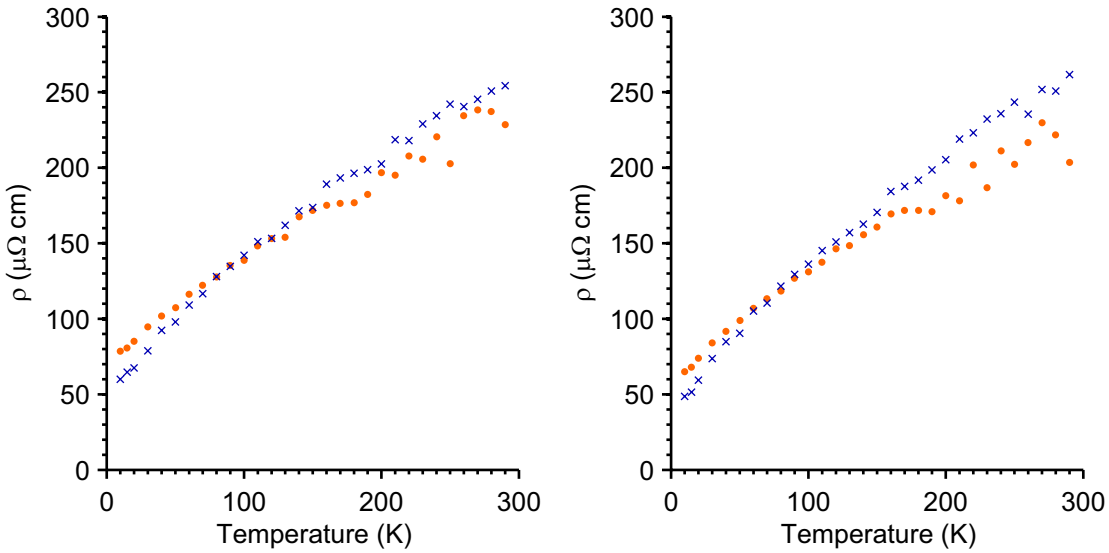

Figure 3.8: Resistivity in $CaRuO_3$ vs. temperature. Left: resistivity extrapolations for CRO-B. Orange dots represent *ab*-plane measurements and blue x's represent *c*-axis measurements. Right: resistivity extrapolations for CRO-H.

we believe that the increase in $\rho\tau^*$ with temperature for $T \gtrsim 100$ is a systematic error, as explained in Section 3.5.

The upturn in $\rho\tau^*$ at low temperatures indicates a reduction in the low-frequency spectral weight. By contrast, Lee *et al.* have reported that the spectral weight below $\Omega_c = 1500\ \mathrm{cm}^{-1}$ actually increases with decreasing temperature [35]. Kamal *et al.* propose two possible explanations for these competing trends in the spectral weight, depending on the model being used [30]. The first is that the scattering rate is strongly anisotropic; the second is that the scattering is frequency-dependent. THz-TDS is an probe of the optical properties of a material, such as the dielectric constant or the optical conductivity. These are second-rank tensors, so while we are able to measure uniaxial transport anisotropy, anisotropies of higher symmetry (such as that in a clover leaf pattern) are not visible. Therefore, neither of the two proposed explanations can be ruled out, as our results only demonstrate that there is little uniaxial anisotropy in the scattering rate.

Other anomalous behaviour in $CaRuO_3$ has been observed before at these temperature scales. Whereas normal Fermi liquid metals exhibit resistivity with a quadratic dependence

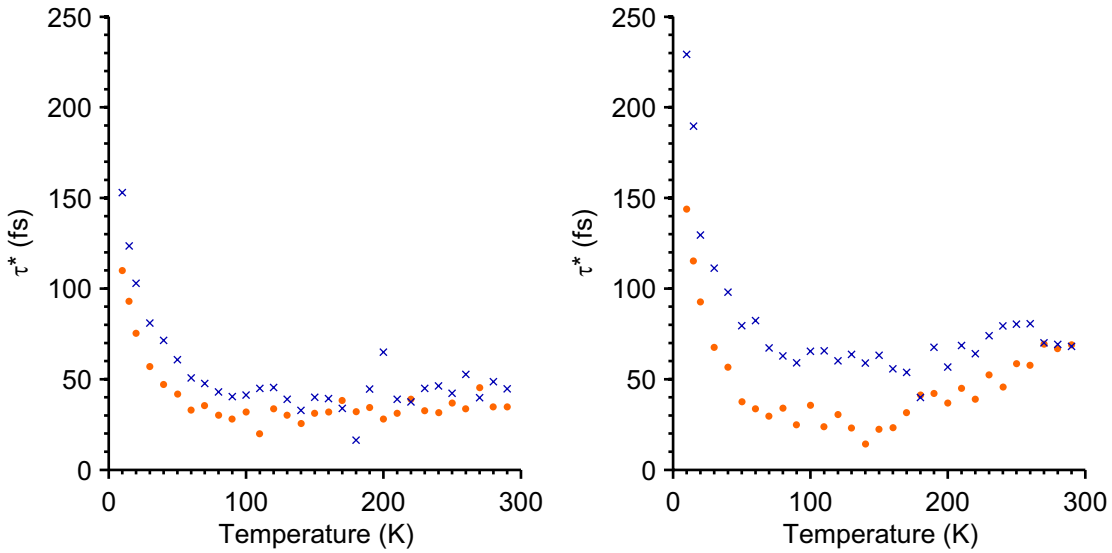

Figure 3.9: Effective scattering lifetime in $CaRuO_3$ vs. temperature. Left: measurements of τ^* for CRO-B. Orange dots represent *ab*-plane measurements and blue x's represent *c*-axis measurements. Right: measurements of τ^* for CRO-H.

on temperature, Klein *et al.* [31] have observed resistivity with a $T^{1.5}$ dependence below $\sim$ 15 K and a $T^{0.5}$ dependence above $\sim$ 40 K. A crossover in the anisotropy of ρ has also be reported below 25 K [44]. Finally, Hall measurements by Gausepohl *et al.* indicate that below 50 K, there is a change from hole-like to electron-like carrier behaviour [26]. The question of whether these changes are related to the low-temperature upturn in the renormalization remains open.

3.5 Importance of substrate matching in $CaRuO_3$

The fact that our renormalization does not flatten out at high temperatures (Figure 3.10) suggests that there may have been systematic error in our substrate mismatch measurements. Before film deposition, the substrates must be characterized for thickness mismatches. Uncertainties in the substrate mismatch directly lead to uncertainties in the scattering lifetime. If a measurement precision of a few femtoseconds is desired, the substrate mismatch must be determined to at least this precision, as can be seen by modulating

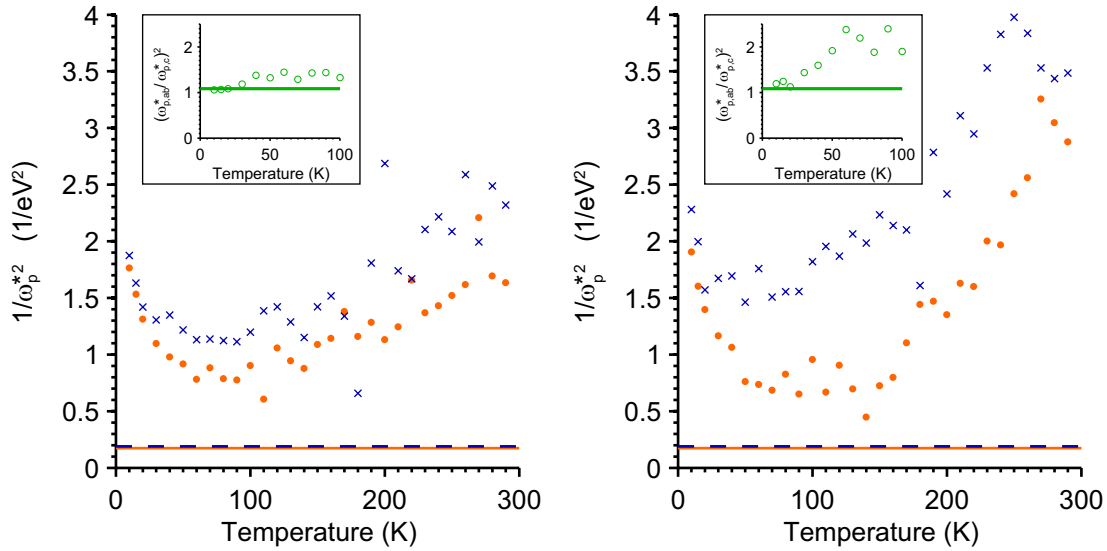

Figure 3.10: Inverse-square plasma frequency measurements for CRO-B (left) and CRO-H (right) vs. temperature. The product $\rho\tau^* = 1/\omega_p^{*2}$ is a measure of the inverse-square plasma frequency and an inverse measure of the spectral weight of the low-frequency Drude peak that appears below 100 K. Data in the *ab*-plane (*c*-axis) is shown as orange dots (blue x's); the band theory prediction [19] is shown as a solid orange (dashed blue) line. Inset: the ratio $(\omega^*_{p,ab}/\omega^*_{p,c})^2$ vs. temperature. Solid line is DFT prediction [19].

Equation 2.13 by a phase $e^{i\omega\eta}$.

The consequences of inaccurate substrate mismatch measurements are shown in Figure 3.11. With the wrong value of η, the temperature dependence of $\rho\tau^*$ can be improbable [the renormalization $(\omega_p/\omega_p^*)^2$ should not increase with temperature in the top data set of Figure 3.11] or impossible (a negative renormalization in the bottom data set). Further evidence of an incorrect substrate mismatch is that our high-temperature scattering lifetime measurements are rather high. However, the relative error in the scattering lifetime is smallest where the scattering lifetime is large, so we have greater confidence in the low-temperature measurements. We have results that demonstrate a lack of transport anisotropy at low temperature, independent of systematic substrate mismatch errors. It would also be good however to record conclusive measurements of τ^* and ω_p^{*2} at higher temperatures. To this end, we sent for new substrates and film samples and began refining our measurements of η in the interim.

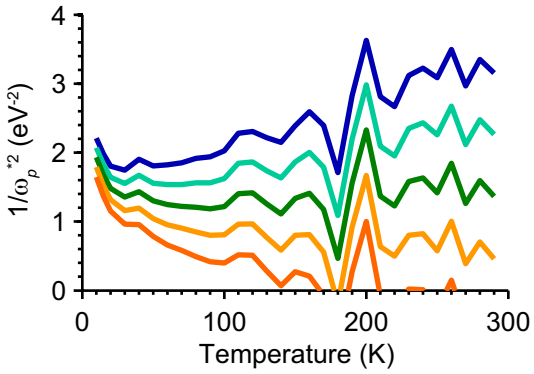

Figure 3.11: The sensitivity of plasma frequency measurements in $CaRuO_3$ to substrate mismatch values. The five sets of data are all taken from the same measurements, but with values of η used in the data analysis that differ by just 10 fs each.

Chapter 4

Experimental improvements

The ability to measure the phase of our transmitted terahertz pulses is of the utmost importance. Indeed, the phase sensitivity of THz-TDS is part of what sets it apart from other spectroscopic techniques that work solely with optical intensities and rely on Kramers-Kronig relations to separate out real and imaginary parts of spectra. In an effort to improve our measurements of the phase of our terahertz pulses, I investigated several sources of systematic error in the phase and whether they could be reduced.

4.1 Sample positioning

Some of the films that we experiment on can only be grown on smaller substrates. Consequently, the aperture upon which we mount these substrates must also be smaller. However, our terahertz beam has a 1/e diameter of up to 8 mm, so smaller apertures can block the outer edges of the beam and/or reshape the pulses. This problem is exacerbated if the terahertz beam does not pass directly through the center of the aperture; incorrect positioning of the apertures in the terahertz beam can easily change the phase slope of the pulses by a few femtoseconds, which in turn changes our scattering lifetime measurements by a similar amount.

The question that we need to solve is, "in what vertical position y does each aperture best transmit the terahertz pulses?" To answer this, we find our reference "null" point, then take THz pulse measurements with the aperture in finely-spaced vertical positions, and then determine which of the positions transmitted the pulse the best. We can use three criteria to judge this:

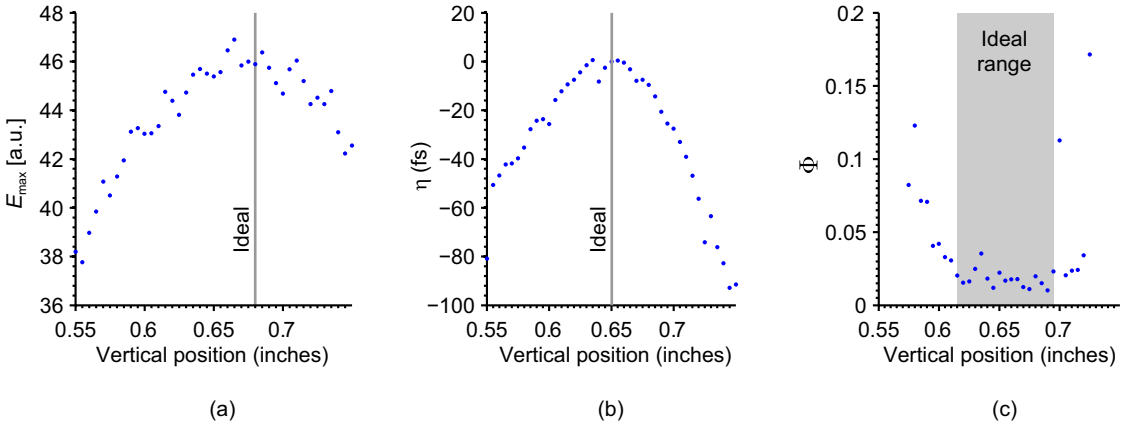

Figure 4.1: Ideal vertical positioning of an 8 mm aperture. Three non-commensurate criteria can be used to judge the ideal vertical position of an aperture. One can look for the position that (a) gives the highest peak terahertz pulse amplitude, (b) impedes the pulse the least (η is a delay time for the pulse arrival at the detector) or (c) has a neighbourhood with the least amount of change in the terahertz pulse spectrum. We choose to follow criterion (b), which is commensurate with the range given by (c).

1. the maximum amplitude of the pulse

2. the pulse delay, i.e. the arrival time of each pulse with respect to a reference pulse

3. the position where the pulse's frequency components are changing the least. This can be quantified by changes in

$$\Phi \equiv \sum_k \left[1 - \left|\frac{\tilde{E}(\omega_k, y + \Delta y)}{\tilde{E}(\omega_k, y)}\right|\right]^2 + \sum_k \left[1 - \left|\frac{\tilde{E}(\omega_k, y)}{\tilde{E}(\omega_k, y - \Delta y)}\right|\right]^2, \tag{4.1}$$

where the ω_k are the discrete frequencies in our measurement bandwidth and $\Delta y = 0.25$" in my measurements.

The values of each of these criteria as a function of position are demonstrated in Figure 4.1 for an 8 mm aperture.

As one can see, the three measures do not all give the same ideal position. The maximum amplitude would appear to be a good measure of the ideal position, as we clearly would like to maximize our signal-to-noise ratio. However, pulse distortion by the aperture edge can reshape the pulse and give it a higher maximum amplitude. Given that our goal is finding the

position that most faithfully transmits the pulse, this would not be ideal. Instead, we settle for a compromise between (2) and (3) above, which are nearly commensurate anyway. The second method measures how much the pulse is impeded or delayed by aperture scattering and the third method measures the minimum amount of pulse distortion by the apertures. With larger apertures, we expect to have flat regions in the plots of Figure 4.1 near the ideal positions, as the transmission of a small beam through a large aperture should be independent of position when the beam and aperture are almost concentric.

4.2 Phase slope instability at low temperatures

We have observed that at low temperatures (below 30 K), measurements of η are unstable. Measurements by Saeid Kamal, a former member of the Dodge Lab, revealed that the optical path length (or phase change) through the cryostat changes as $m^{(\eta)}/T$, where T is the temperature inside the cryostat and $m^{(\eta)} = 2570$ fs $\cdot$ K. At low temperatures, the optical thickness between two measurements thus becomes highly sensitive to temperature fluctuations. If two transmission measurements (i.e. through sample and reference) are not taken at exactly the same temperature, the optical thickness between the two terahertz pulses will be artificially altered by $\Delta\eta \propto \Delta T/T^2$. This may be the cause of the low-temperature deviations in the $NdGaO_3$ substrate mismatch measurements of Figure 3.4. Removing this source of uncertainty would allow us to lower the temperature range over which we can make measurements, getting us closer to simulating ground-state transport conditions.

This $1/T$ behaviour is suggestive of a Curie law phenomenon, where a paramagnetic or paraelectric material in the path of the terahertz pulse is becoming more magnetized/polarized with decreasing temperature. Consequently, I conducted experiments to investigate two potential "Curie candidates".

4.2.1 Curie candidate 1: Oxygen in vacuum jacket

The only substances in the THz beam's path that are cooled to such low temperatures are the inner Mylar windows on the cryostat, the contents of the cryostat sample chamber (assumed to be 100% helium after two hours of cooling down), and whatever gas remains in the cryostat vacuum jacket, which is typically pumped down to between 0.04 and 1 mtorr. Oxygen is a well-known paramagnet, so we suspected that there may be residual oxygen in

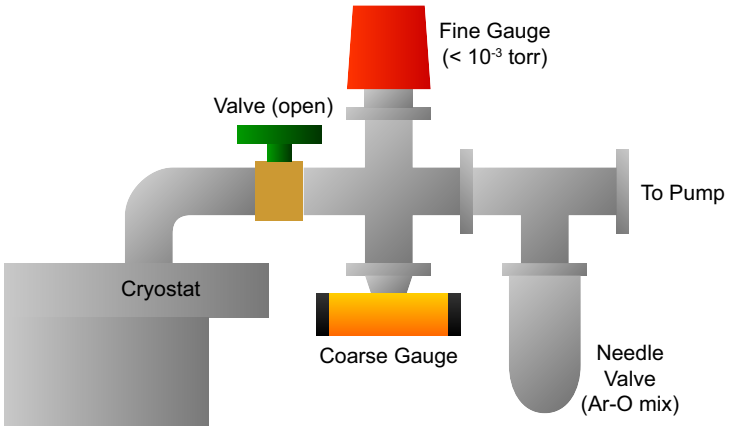

Figure 4.2: The assembly used to inject the argon-oxygen mixture into the cryostat.

the 'vacuum' that is causing the problem.

To test this hypothesis, I attached the assembly in Figure 4.2 to the vacuum jacket control valve. The assembly consisted of fine and coarse pressure gauges, a needle valve to insert a mixture of argon and oxygen (95% and 5%, respectively) into the jacket, and an outlet to pump the jacket down. I pumped our cryostat's vacuum chamber down to a pressure of 0.04 mtorr and made terahertz transmission measurements through an empty 10 mm aperture at temperatures of $T = 8, 10, 20, 50, 100,$ and 160 K. The argon-oxygen mixture was then injected into the vacuum such that the pressure was increased to 1 mtorr, and the transmission measurements were repeated. Further measurements were made with a vacuum chamber pressure of 8 mtorr.

The presence of oxygen in the vacuum chamber was our main candidate for the observed $1/T$ behaviour. In an unbaked vacuum with a leak, oxygen makes up about 1% of the vacuum's composition. Thus, in a 0.04 mtorr environment, we have 4×10^{-7} torr of oxygen. When we introduce 8 mtorr of our argon-oxygen mixture, we have about 4×10^{-4} torr of oxygen, or a 1000-fold increase in oxygen content. However, despite this enormous increase in the gaseous contents of the vacuum chamber, the $1/T$ response was not amplified. Figure 4.3 demonstrates the independence of the $1/T$ response from the vacuum chamber pressure (at least in terms of the change we expect from such a large increase in oxygen content). The pressure measurement is not precise because it had to be made through an open valve, which would inherently have a pressure gradient across it. However, such a pressure gradient would

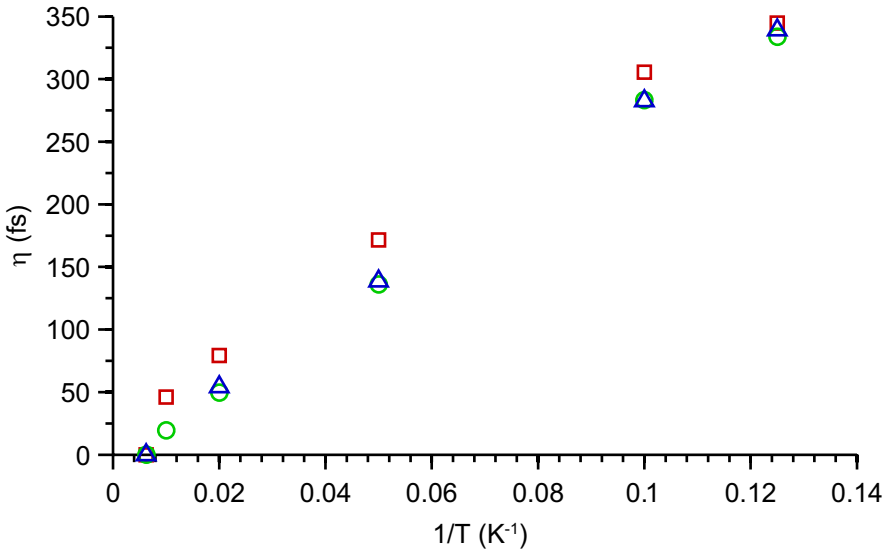

Figure 4.3: The optical thickness of the cryostat with respect to its thickness at high temperature, versus inverse temperature. Measurements were taken with vacuum jacket pressures of 0.04 mtorr (red squares), 1 mtorr (green circles), and 8 mtorr (blue triangles). The $1/T$ behaviour is clear, but the effect seems to be independent of the vacuum jacket's gaseous contents.

only mean that the pressure in the cryostat would be higher than the pressure measured at the gauge, so our conclusion that the $1/T$ response is independent of pressure still holds. It seems that while it is important to have a good vacuum in the cryostat jacket for thermal insulation, small amounts of gas in the jacket do not affect the optical properties of the cryostat.

4.2.2 Curie candidate 2: Inner Mylar windows

Having ruled out a $1/T$ contribution from stray oxygen, my focus then turned to whether the cold inner Mylar windows could be causing the problem and whether other commonly-used terahertz windows exhibited such $1/T$ behaviour. Preliminary THz-TDS measurements on a 100 μm film of Mylar revealed that its optical thickness indeed showed a $1/T$ behaviour. We requested a $15 \times 15 \times 2$ mm sample of Mylar (high-density polyethylene, HDPE) from Tydex, as well as samples of polypropylene (PP), polymethylpentene (TPX), and Topas Cyclic Olefin Copolymers (TC) from Tydex and a sample of tsurupica from Microtech. All

five of these materials are polymers.

As can be seen in Figure 4.4, the terahertz refractive indices n (and hence the phase changes they induce) of all five polymer windows change as $1/T$ below 20 K. The refractive index slope $m^{(n)}$ of Mylar is -0.127 K, while the rest of the slopes lie between -0.026 K (Tsurupica) and -0.177 K (polypropylene). We can convert the slope in n to a slope in η: $m^{(\eta)} = \frac{d}{c} m^{(n)}$ to try to identify the cause of the $1/T$ as the Mylar windows, using $d = 2 \times 0.01$", the total thickness of our two inner Mylar windows. Unfortunately, this gives a Mylar slope of $m^{(\eta)} = -215$ fs $\cdot$ K — a large discrepancy in both sign and magnitude from the aforementioned measurements by Saeid Kamal and the slopes in Figure 4.3 (which are also around 2500 fs $\cdot$ K). It seems that the Mylar windows are not the cause of the $1/T$ effect.

4.2.3 Discussion

While the issue of the $1/T$ behaviour was not resolved here, the hypotheses of oxygen in the cryostat vacuum jacket and inappropriate window materials seem to have lost credibility. Hopefully future experiments can identify the cause of this effect so that lower-temperature measurements can be more easily taken.

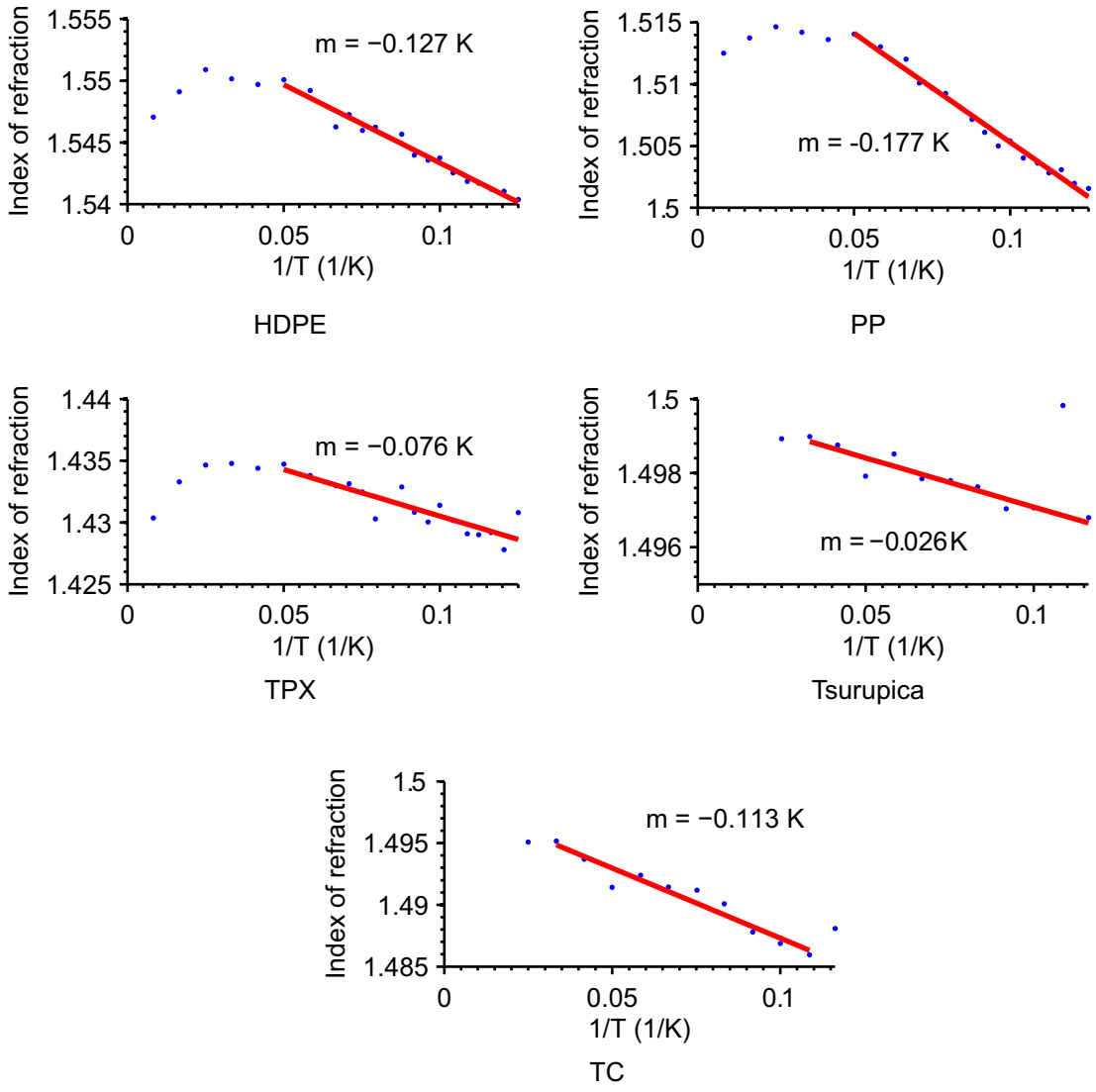

Figure 4.4: Index of refraction vs. $1/T$ for five window materials. Measurements of Mylar (HDPE), polypropylene (PP), polymethylpentene (TPX), Tsurupica, and Topas Cyclic Olefin Copolymers (TC) are shown. Linear regressions are fit to measurements taken at $T \leq 20$ K, with the slopes $m = m^{(n)}$ noted in each plot.

Chapter 5

Future directions

This thesis has emphasized the importance of the probing pulse phase measurement for scattering lifetime measurements using terahertz time-domain spectroscopy. Here I outline what can be done in the future with the work presented in this thesis.

5.1 Calcium ruthenate

While there seems to be systematic error in the $CaRuO_3$ scattering lifetime measurements presented here, the effect of this error on the plasma frequency measurements decreases at low temperature. Therefore, we can be confident that any plasma frequency anisotropy near the ground state is weak.

Further measurements on $CaRuO_3$ with higher levels of phase measurement precision could characterize its scattering lifetime and plasma frequency at higher temperatures. I have characterized more $NdGaO_3$ substrates, the results of which are in Appendix A. It would have been advantageous to pursue this and to take the new $CaRuO_3$ measurements within the context of this thesis, but due to technical difficulties in the film-grower's laboratory, further samples were unavailable during our timeline.

5.2 Phase measurements

Future measurements with this THz-TDS setup should incorporate the improvements on the experimental technique I have outline here. Namely,

1. the existence of mechanical hysteresis in the sample stick motion implies that the null point must be found every time that the stick's direction of motion is changed

2. the ideal vertical positions of the aperture should be determined by the methods of Section 4.1.

While the influence of polymer windows on the aforementioned $1/T$ behaviour seems small, non-polymer window materials might also be investigated to see whether the behaviour is seen in the cryostat thickness.

5.3 Sample constraints

I have observed that most of the noise in our terahertz pulses is multiplicative, so we should be able to measure conductivity in relatively opaque films with our THz-TDS setup, whether this opacity is due to the materials' conductivity or the films' thickness. Using the measurements of the frequency-domain noise floor in this thesis, we can predict what materials we can study, given a frequency range of interest and a desired signal to noise ratio.

Appendix A

New substrate mismatch measurements

In preparation for future transport measurements of calcium ruthenate films, I characterized three more $NdGaO_3$ substrates: NGO-A, NGO-B (unrelated to the NGO-B substrate used in Chapter 3), and NGO-I. The miscut of these substrates was 4° in the $[\bar{1}10]$ direction, as opposed to the 0.15° miscut of the previous substrates. We hope that this will improve film quality even further. In these measurements, the optical thicknesses of NGO-A and NGO-I were compared to that of NGO-B at several temperatures. The substrates were mounted identically to those described in Chapter 3.

I present the results in Tables A.1 and A.2. For increased certainty in the results, I repeated each measurement of η N times. The unbiased standard deviation of each measurement is listed as σ and the uncertainty in the mismatch is approximated as $\sigma/\sqrt{N}$. I plot these tables in Figures A.1 and A.2. Beyond the fluctuations that are characterized by the various values of σ, one can expect a variation of up to 4 fs with subsequent measurements of η if the samples are remounted or repeatedly cooled down. However, the experiment-by-experiment measurements only vary by 1–2 fs in the majority of cases.

Table A.1: The substrate mismatch for measurements in the *ab*-plane, η_{ab}. Subscripts AB and IB refer to measurements of substrates NGO-A and NGO-I with respect to substrate NGO-B, respectively.

Temperature (K)	N	η_{AB} (fs)	$\frac{\sigma_{\mathrm{AB}}}{\sqrt{N}}$ (fs)	σ_{AB} (fs)	η_{IB} (fs)	$\frac{\sigma_{\mathrm{IB}}}{\sqrt{N}}$ (fs)	σ_{IB} (fs)
40	5	-13.1	1.7	3.8	-7.1	0.7	1.5
100	4	-14.3	1.2	2.5	-11.0	3.1	6.2
150	3	-16.1	1.1	1.8	-2.0	1.8	3.0
225	3	-15.5	3.1	5.4	-10.6	1.3	2.3
292	93	-21.3	0.4	3.9	-8.7	0.4	3.9

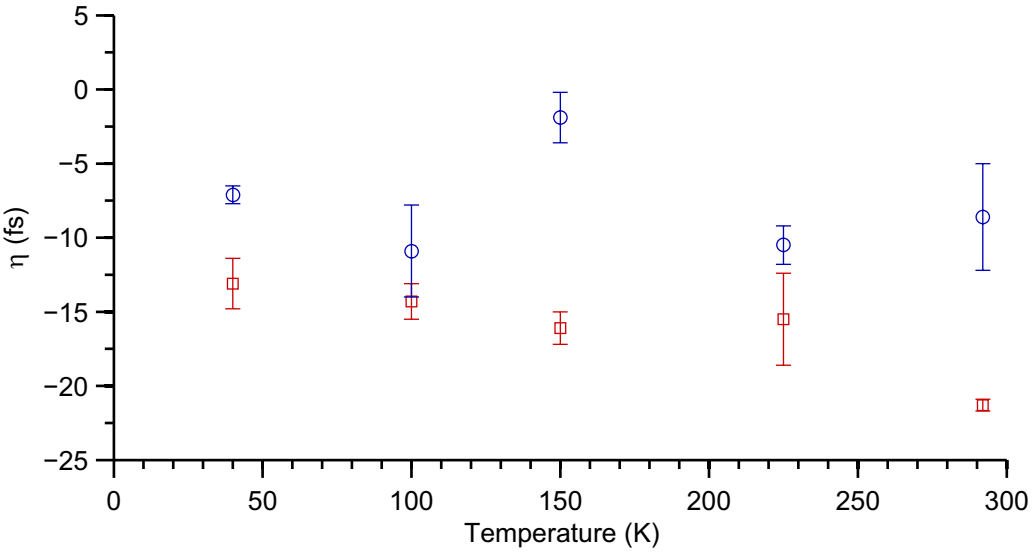

Figure A.1: Basal (*ab*-plane) substrate mismatch of NGO-A (red squares) and NGO-I (blue circles) with respect to NGO-B, versus temperature. Error bars taken from $\sigma/\sqrt{N}$.

Table A.2: The substrate mismatch for measurements in the c-axis, η_c. Subscripts AB and IB refer to measurements of substrates NGO-A and NGO-I with respect to substrate NGO-B, respectively.

Temperature (K)	N	η_{AB} (fs)	$\frac{\sigma_{\mathrm{AB}}}{\sqrt{N}}$ (fs)	σ_{AB} (fs)	η_{IB} (fs)	$\frac{\sigma_{\mathrm{IB}}}{\sqrt{N}}$ (fs)	σ_{IB} (fs)
40	3	-0.1	1.2	2.1	9.3	1.1	1.9
100	3	0.3	0.6	1.0	9.0	1.1	1.9
150	3	0.9	1.3	2.3	6.5	1.9	3.2
225	2	5.1	0.7	1.0	14.3	1.4	1.9
260	3	6.6	2.0	3.5	18.5	0.9	1.5
292	79	7.4	0.5	4.1	22.0	0.6	5.4

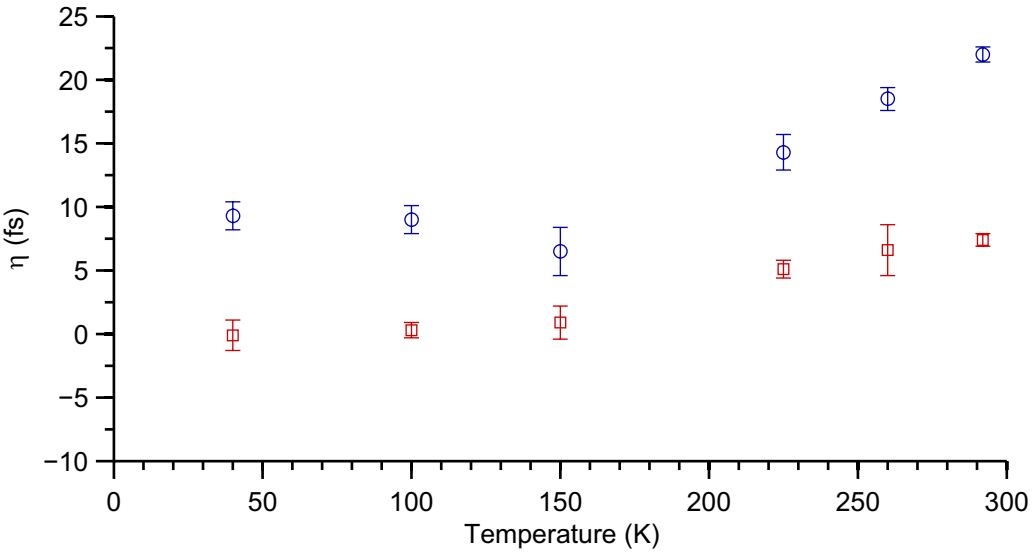

Figure A.2: Perpendicular (c-axis) substrate mismatch of NGO-A (red squares) and NGO-I (blue circles) with respect to NGO-B, versus temperature. Error bars taken from $\sigma/\sqrt{N}$.

Bibliography

[1] Neil W. Ashcroft and N. David Mermin. *Solid State Physics*. Saunders College, 1976.

[2] D. H. Auston, K. P. Cheung, and P. R. Smith. Picosecond photoconducting hertzian dipoles. *Applied Physics Letters*, 45:284–286, 1984.

[3] R. J. Barlow. *Statistics: A guide to the Use of Statistical Methods in the Physical Sciences*. John Wiley & Sons Ltd., 1989.

[4] D. N. Basov and T. Timusk. Electrodynamics of high-T_c superconductors. *Reviews of Modern Physics*, 77:721, 2005.

[5] P. D. Battle and W. J. Macklin. The crystal and magnetic structures of Sr_2YRuO_6. *Journal of Solid State Chemistry*, 52:138 – 145, 1984.

[6] R.J. Bouchard and J.L. Gillson. Electrical properties of $CaRuO_3$ and $SrRuO_3$ single crystals. *Materials Research Bulletin*, 7:873 – 878, 1972.

[7] Alan Callaghan, Carl W. Moeller, and Roland Ward. Magnetic interactions in ternary ruthenium oxides. *Inorganic Chemistry*, 5:1572–1576, 1966.

[8] P. Calvani, M. Capizzi, F. Donato, P. Dore, S. Lupi, P. Maselli, and C.P. Varsamis. Infrared optical properties of perovskite substrates for high-t_c superconducting films. *Physica C: Superconductivity*, 181:289–295, 1991.

[9] G. Cao, S. McCall, M. Shepard, J. E. Crow, and R. P. Guertin. Thermal, magnetic, and transport properties of single-crystal $Sr_{1-x}Ca_xRuO_3$ ($0 \leq x \leq 1$). *Physical Review B*, 56:321–329, Jul 1997.

[10] R. J. Cava. Schizophrenic electrons in ruthenium-based oxides. *Dalton Transactions*, 19:2979–2987, 2004.

[11] John Frederick Corson. *Advances in Terahertz Spectroscopy of High-T_c Superconductors*. PhD thesis, University of California at Berkeley, 2000.

[12] L. Degiorgi. The electrodynamic response of heavy-electron compounds. *Reviews of Modern Physics*, 71:687–734, Apr 1999.

[13] Susan L. Dexheimer, editor. *Terahertz Spectroscopy: Principles and Applications*. CRC Press, 2008.

[14] F.E. Doany, D. Grischkowsky, and C.-C. Chi. Carrier lifetime versus ion-implantation dose in silicon on sapphire. *Applied Physics Letters*, 50:460–462, 1987.

[15] J. S. Dodge, C. P. Weber, J. Corson, J. Orenstein, Z. Schlesinger, J. W. Reiner, and M. R. Beasley. Low-frequency crossover of the fractional power-law conductivity in $SrRuO_3$. *Physical Review Letters*, 85:4932–4935, Dec 2000.

[16] J.S. Dodge, J. Corson, R. Mallozzi, J. Orenstein, J. Reiner, and M.R. Beasley. Electron-magnon renormalization effects in $SrRuO_3$. In *Quantum Electronics and Laser Science Conference, 1999. QELS '99. Technical Digest. Summaries of Papers Presented at the*, pages 212–213, May 1999.

[17] S. V. Dordevic, D. N. Basov, N. R. Dilley, E. D. Bauer, and M. B. Maple. Hybridization gap in heavy fermion compounds. *Physical Review Letters*, 86:684–687, Jan 2001.

[18] Lionel Duvillaret, Frédéric Garet, and Jean-Louis Coutaz. Highly precise determination of optical constants and sample thickness in terahertz time-domain spectroscopy. *Applied Optics*, 38:409–415, 1999.

[19] Ilya Elfimov, 2010. Private communication.

[20] C. B. Eom, R. J. Cava, R. M. Fleming, Julia M. Phillips, R. B. vanDover, J. H. Marshall, J. W. P. Hsu, J. J. Krajewski, and Jr. Peck, W. F. Single-crystal epitaxial thin films of the isotropic metallic oxides $Sr_{1-x}Ca_xRuO_3$ ($0 \leq x \leq 1$). *Science*, 258:1766–1769, 1992.

[21] C. B. Eom, J. Z. Sun, K. Yamamoto, A. F. Marshall, K. E. Luther, T. H. Geballe, and S. S. Laderman. In situ grown $YBa_2Cu_3O_{7-d}$ thin films from single-target magnetron sputtering. *Applied Physics Letters*, 55:595–597, 1989.

[22] Ch. Fattinger and D. Grischkowsky. Point source terahertz optics. *Applied Physics Letters*, 53:1480, 1988.

[23] Ch. Fattinger and D. Grischkowsky. Terahertz beams. *Applied Physics Letters*, 54:490–492, 1989.

[24] Fumihiko Fukunaga and Nobuo Tsuda. On the magnetism and electronic conduction of itinerant magnetic system $Ca_{1-x}Sr_xRuO_3$. *Journal of the Physical Society of Japan*, 63:3798–3807, 1994.

[25] Q. Gan, R. A. Rao, and C. B. Eom. Control of the growth and domain structure of epitaxial $SrRuO_3$ thin films by vicinal (001) $SrTiO_3$ substrates. *Applied Physics Letters*, 70:1962–1964, 1997.

[26] S. C. Gausepohl, Mark Lee, R. A. Rao, and C. B. Eom. Hall-effect sign reversal in $CaRuO_3$ and $SrRuO_3$ thin films. *Physical Review B*, 54:8996–8999, Oct 1996.

[27] T. C. Gibb, R. Greatrex, N. N. Greenwood, and P. Kaspi. Ruthenium-99 Mössbauer studies of the magnetic properties of ternary and quaternary ruthenium(IV) oxides. *Journal of the Chemical Society, Dalton Transactions*, 1973:1253, 1973.

[28] M. A. Gilmore, Saeid Kamal, D. M. Broun, and J. S. Dodge. Determination of electron-phonon interaction parameters from time-domain terahertz spectroscopy. *Applied Physics Letters*, 88:141910, 2006.

[29] D. Grischkowsky, Søren Keiding, Martin van Exter, and Ch. Fattinger. Far-infrared time-domain spectroscopy with terahertz beams of dielectrics and semiconductors. *Journal of the Optical Society of America B*, 7:2006–2015, 1990.

[30] Saeid Kamal, D. M. Kim, C. B. Eom, and J. S. Dodge. Terahertz-frequency carrier dynamics and spectral weight redistribution in the nearly magnetic metal $CaRuO_3$. *Physical Review B*, 74:165115, 2006.

[31] L. Klein, L. Antognazza, T. H. Geballe, M. R. Beasley, and A. Kapitulnik. Possible non-fermi-liquid behavior of $CaRuO_3$. *Physical Review B*, 60:1448–1451, Jul 1999.

[32] H. Kobayashi, M. Nagata, R. Kanno, and Y. Kawamoto. Structural characterization of the orthorhombic perovskites: [$ARuO_3$ A = Ca, Sr, La, Pr)]. *Materials Research Bulletin*, 29:1271 – 1280, 1994.

[33] P. Kostic, Y. Okada, N. C. Collins, Z. Schlesinger, J. W. Reiner, L. Klein, A. Kapitulnik, T. H. Geballe, and M. R. Beasley. Non-fermi-liquid behavior of $SrRuO_3$: Evidence from infrared conductivity. *Physical Review Letters*, 81:2498–2501, Sep 1998.

[34] Carl-Philippe Kübler. Creation and characterization of a terahertz time-domain spectrometer. Master's thesis, Simon Fraser University, 2002.

[35] Y. S. Lee, Jaejun Yu, J. S. Lee, T. W. Noh, T.-H. Gimm, Han-Yong Choi, and C. B. Eom. Non-Fermi liquid behavior and scaling of the low-frequency suppression in the optical conductivity spectra of $CaRuO_3$. *Physical Review B*, 66:041104, Jul 2002.

[36] J. M. Longo, P. M. Raccah, and J. B. Goodenough. Magnetic properties of $SrRuO_3$ and $CaRuO_3$. *Journal of Applied Physics*, 39:1327–1328, 1968.

[37] Christoph Ludwig, Jrgen Kuhl, and Jeffrey O. White. Complex dielectric function of $NdGaO_3$ in the THz frequency regime. *Optics Communications*, 134:95–98, 1997.

[38] Y. Maeno, H. Hashimoto, K. Yoshida, S. Nishizaki, T. Fujita, J. G. Bednorz, and F. Lichtenberg. Superconductivity in a layered perovskite without copper. *Nature*, 372:532–534, Dec 1994.

[39] Jon-Paul Maria, H. L. McKinstry, and S. Trolier-McKinstry. Origin of preferential orthorhombic twinning in $SrRuO_3$ epitaxial thin films. *Applied Physics Letters*, 76:3382–3384, 2000.

[40] I. I. Mazin and D. J. Singh. Electronic structure and magnetism in Ru-based perovskites. *Physical Review B*, 56:2556–2571, Aug 1997. **73**:189903(E) (2006).

[41] F. Nakamura, Y. Senoo, T. Goko, M. Ito, T. Suzuki, S. Nakatsuji, H. Fukazawa, Y. Maeno, P. Alireza, and S. R. Julian. Pressure-induced ferromagnetic metal for a Mott insulator Ca_2RuO_4. *Physica B: Condensed Matter*, 329-333:803 – 804, 2003. Proceedings of the 23rd International Conference on Low Temperature Physics.

[42] Satoru Nakatsuji, Shin-Ichi Ikeda, and Yoshiteru Maeno. Ca_2RuO_4: New Mott insulators of layered ruthenate. *Journal of the Physical Society of Japan*, 66:1868–1871, 1997.

[43] Martin C. Nuss and Joseph Orenstein. *Millimeter and Submillimeter Wave Spectroscopy of Solids*. Springer-Verlag Berlin Heidelberg, 1998.

[44] D. L. Proffit, H. W. Jang, S. Lee, C. T. Nelson, X. Q. Pan, M. S. Rzchowski, and C. B. Eom. Influence of symmetry mismatch on heteroepitaxial growth of perovskite thin films. *Applied Physics Letters*, 93:111912, 2008.

[45] John J. Randall and Roland Ward. The preparation of some ternary oxides of the platinum metals. *Journal of the American Chemical Society*, 81:2629–2631, 1959.

[46] G Santi and T Jarlborg. Calculation of the electronic structure and the magnetic properties of $SrRuO_3$ and $CaRuO_3$. *Journal of Physics: Condensed Matter*, 9:9563–9584, 1997.

[47] Moty Schultz, Lior Klein, J. W. Reiner, and M. R. Beasley. Uniaxial magnetocrystalline anisotropy in $CaRuO_3$. *Physical Review B*, 73:085109, 2006.

[48] A. E. Siegman. *Lasers*. University Science Books, 1986.

[49] D. J. Singh and I. I. Mazin. *Ruthenate and Rutheno-Cuprate Materials*, pages 256–270. Springer, Berlin, 2002.

[50] David J. Singh. Electronic and magnetic properties of the 4d itinerant ferromagnet $SrRuO_3$. In *The 40th annual conference on magnetism and magnetic materials*, volume 79, pages 4818–4820. AIP, 1996.

[51] P. R. Smith and D. H. Auston. Subpicosecond photoconducting dipole antennas. *IEEE Journal of Quantum Electronics*, 24:255–260, 1988.